

FACULTY  
OF MATHEMATICS  
AND PHYSICS  
Charles University

1

BACHELOR THESIS

2

Martin Vavřík

3

**Simulation and Reconstruction  
of Charged Particle Trajectories  
in an Atypic Time Projection Chamber**

4

5

Institute of Particle and Nuclear Physics

6

Supervisor of the bachelor thesis: Mgr. Tomáš Sýkora, Ph.D.

7

Study programme: Physics

8

Prague 2025

- <sup>9</sup> I declare that I carried out this bachelor thesis independently, and only with the  
<sup>10</sup> cited sources, literature and other professional sources. It has not been used to  
<sup>11</sup> obtain another or the same degree.
- <sup>12</sup> I understand that my work relates to the rights and obligations under the Act  
<sup>13</sup> No. 121/2000 Sb., the Copyright Act, as amended, in particular the fact that the  
<sup>14</sup> Charles University has the right to conclude a license agreement on the use of this  
<sup>15</sup> work as a school work pursuant to Section 60 subsection 1 of the Copyright Act.

In ..... date .....  
Author's signature



Title: Simulation and Reconstruction of Charged Particle Trajectories in an Atypical Time Projection Chamber **Added hyphen to avoid overfull hbox**

Author: Martin Vavřík

Institute: Institute of Particle and Nuclear Physics

Supervisor: Mgr. Tomáš Sýkora, Ph.D., Institute of Particle and Nuclear Physics

Abstract: Abstract.

Keywords: key words

# <sup>17</sup> Contents

<sup>18</sup>	<b>Motivation</b>	<sup>3</sup>
<sup>19</sup>	0.1 ATOMKI Anomaly . . . . .	<sup>3</sup>
<sup>20</sup>	0.1.1 ATOMKI Measurements . . . . .	<sup>3</sup>
<sup>21</sup>	0.1.2 Other Experiments . . . . .	<sup>4</sup>
<sup>22</sup>	0.2 X17 Project at IEAP CTU . . . . .	<sup>6</sup>
<sup>23</sup>	<b>1 Time Projection Chamber</b>	<sup>9</sup>
<sup>24</sup>	1.1 Charge transport in gases . . . . .	<sup>9</sup>
<sup>25</sup>	1.1.1 Drift . . . . .	<sup>9</sup>
<sup>26</sup>	1.1.2 Diffusion . . . . .	<sup>11</sup>
<sup>27</sup>	1.2 Readout . . . . .	<sup>12</sup>
<sup>28</sup>	1.2.1 Multi-Wire Proportional Chamber . . . . .	<sup>12</sup>
<sup>29</sup>	1.2.2 Gas Electron Multiplier . . . . .	<sup>12</sup>
<sup>30</sup>	1.2.3 Micromegas . . . . .	<sup>12</sup>
<sup>31</sup>	1.2.4 Parallel Plate Chamber . . . . .	<sup>13</sup>
<sup>32</sup>	1.3 Orthogonal Fields TPC at IEAP CTU . . . . .	<sup>13</sup>
<sup>33</sup>	1.3.1 Motivation and Associated Challenges . . . . .	<sup>13</sup>
<sup>34</sup>	1.3.2 Coordinate Systems and Dimensions . . . . .	<sup>14</sup>
<sup>35</sup>	1.3.3 Magnetic Field Simulation . . . . .	<sup>16</sup>
<sup>36</sup>	<b>2 Track Simulation</b>	<sup>19</sup>
<sup>37</sup>	2.1 Microscopic Simulation . . . . .	<sup>19</sup>
<sup>38</sup>	2.1.1 First testing track . . . . .	<sup>20</sup>
<sup>39</sup>	2.1.2 Grid-like testing sample . . . . .	<sup>20</sup>
<sup>40</sup>	2.2 Runge-Kutta Simulation . . . . .	<sup>20</sup>
<sup>41</sup>	2.2.1 Testing sample . . . . .	<sup>23</sup>
<sup>42</sup>	<b>3 Track Reconstruction</b>	<sup>25</sup>
<sup>43</sup>	3.1 Reconstruction Assuming Steady Drift . . . . .	<sup>25</sup>
<sup>44</sup>	3.2 Ionization Electron Map . . . . .	<sup>26</sup>
<sup>45</sup>	3.2.1 Gradient Descent Algorithm . . . . .	<sup>30</sup>
<sup>46</sup>	3.2.2 Interpolation on the Inverse Grid . . . . .	<sup>31</sup>
<sup>47</sup>	3.3 Discrete Reconstruction . . . . .	<sup>33</sup>
<sup>48</sup>	<b>4 Energy Reconstruction</b>	<sup>35</sup>
<sup>49</sup>	4.1 Cubic Spline Fit . . . . .	<sup>35</sup>
<sup>50</sup>	4.2 Circle and Lines Fit . . . . .	<sup>37</sup>
<sup>51</sup>	4.2.1 Two-dimensional fit . . . . .	<sup>38</sup>
<sup>52</sup>	4.2.2 Three-dimensional fit . . . . .	<sup>39</sup>
<sup>53</sup>	4.2.3 Testing on a Runge-Kutta sample . . . . .	<sup>41</sup>
<sup>54</sup>	4.3 Runge-Kutta Fit . . . . .	<sup>42</sup>
<sup>55</sup>	4.3.1 Testing on a microscopic sample . . . . .	<sup>44</sup>
<sup>56</sup>	<b>Conclusion</b>	<sup>46</sup>
<sup>57</sup>	<b>Bibliography</b>	<sup>49</sup>



# <sup>59</sup> Motivation

<sup>60</sup> A Time Projection Chamber (TPC) [refs] is a type of gaseous detector that detects  
<sup>61</sup> charged particle trajectories by measuring the positions and drift time of ions cre-  
<sup>62</sup> ated in the gas. The energies of these particles can be inferred from the curvatures  
<sup>63</sup> of their trajectories in the magnetic field (specific field inside the TPC).

<sup>64</sup> The goal of this thesis is to develop an algorithm for the reconstruction of  
<sup>65</sup> charged particle trajectories and energy in an *atypic* TPC with orthogonal elec-  
<sup>66</sup> tric and magnetic fields, hereafter referred to as the Orthogonal Fields TPC  
<sup>67</sup> (OFTPC), used in the X17 project at the Institute of Experimental and Ap-  
<sup>68</sup> plied Physics, Czech Technical University in Prague (IEAP CTU). Furthermore,  
<sup>69</sup> we present the results of testing of several (gradually improving) developed algo-  
<sup>70</sup> rithms with different samples of simulated data. Put this somewhere, (maybe just  
<sup>71</sup> the abstract?). We use the Garfield++ toolkit [1] for simulations in combination  
<sup>72</sup> with the ROOT framework [2] for data analysis and visualization. Some of our  
<sup>73</sup> more demanding simulations are run on the MetaCentrum grid [3].

<sup>74</sup> The X17 project in IEAP CTU aims to reproduce measurements of anomalous  
<sup>75</sup> behavior in the angular correlation distribution of pairs produced by the Internal  
<sup>76</sup> Pair Creation (IPC) mechanism [4] during the decay of certain excited nuclei  
<sup>77</sup> (<sup>8</sup>Be, <sup>12</sup>C, and <sup>4</sup>He) observed by a team at ATOMKI in Hungary. I would leave  
<sup>78</sup> this here as a short summary before I explain it in more detail in the sections  
<sup>79</sup> below.

<sup>80</sup> Add citations: X17 project, VdG. Maybe also TPC, etc.

## <sup>81</sup> 0.1 ATOMKI Anomaly

<sup>82</sup> Many different theories propose the existence of *new light boson(s)* that are weakly  
<sup>83</sup> coupled to ordinary matter [5]. These particles are potential dark matter candi-  
<sup>84</sup> dates and could contribute to a solution of other issues with the Standard Model,  
<sup>85</sup> such as the strong CP problem and the anomalous muon magnetic moment. Mass  
<sup>86</sup> range of axions?

<sup>87</sup> A possible way of detecting such bosons with a short lifetime is to observe  
<sup>88</sup> nuclear transitions of excited nuclei. If a boson was emitted during the transition  
<sup>89</sup> and subsequently decayed into an electron-positron pair, we could observe this as  
<sup>90</sup> a peak on top of the standard  $e^+e^-$  (both cursive and upright forms are used in  
<sup>91</sup> different articles) angular correlation from the Internal Pair Creation (IPC) and  
<sup>92</sup> the External Pair Creation (EPC).

### <sup>93</sup> 0.1.1 ATOMKI Measurements

<sup>94</sup> Historically, there were several measurements of the IPC in nuclear transitions  
<sup>95</sup> in <sup>8</sup>Be at Institute für Kernphysik (Frankfurt) [6, 7, 8] and at ATOMKI (De-  
<sup>96</sup> brecen, Hungary) [9, 10] resulting in different anomalies with invariant mass in  
<sup>97</sup> the range 5 – 15 MeV. This prompted a development of a better spectrometer at  
<sup>98</sup> ATOMKI.

<sup>99</sup> In 2015, a group at ATOMKI observed an anomalous IPC in <sup>8</sup>Be [11]. They  
<sup>100</sup> used the  ${}^7\text{Li}(p, \gamma){}^8\text{Be}$  reaction at the  $E_p = 1030$  keV proton capture resonance

to prepare the 18.15 MeV excited state ( $J^\pi = 1^+$ ,  $T = 0$ ). This state decays predominantly through M1 transitions to the ground state ( $J^\pi = 0^+$ ,  $T = 0$ ) and to the 3.03 MeV state ( $J^\pi = 2^+$ ,  $T = 0$ ) [12]. **Transition figure – all transitions of isotopes? IPC figure?**

The angular correlation of the  $e^+e^-$  pairs created internally in these transitions were measured and compared to the simulation; results from a narrow  $E_{\text{sum}} = 18$  MeV region are shown in Figure 0.1a. The simulation includes boson decay pairs for different boson masses. The disparity parameter  $y$  is defined as

$$y = \frac{E_{e^-} - E_{e^+}}{E_{e^-} + E_{e^+}}, \quad (0.1)$$

where  $E_{e^-}$  and  $E_{e^+}$  are the kinetic energies of the electron and positron.

Their experimental setup was later upgraded (**details?**) and used for new measurements. In 2022 the  ${}^8\text{Be}$  anomaly was also measured using the  $E_p = 441$  keV resonance to produce the 17.64 MeV excited state ( $J^\pi = 1^+$ ,  $T = 1$ ) which again decays primarily to the ground state and the 3.03 MeV state [12]. The anomaly was also measured for  $E_p = 650$  and 800 keV where E1 transitions from the direct proton capture dominate [13]. The results for  $e^+e^-$  with  $E_{\text{sum}} \in [13.5, 20]$  MeV are shown in Figure 0.1b.

The newer setup was also used in 2021 to study the  ${}^3\text{H}(p, e^+e^-){}^4\text{He}$  reaction at  $E_p = 510, 610$  and 900 keV [14], inducing direct and resonant capture populating the overlapping first 20.21 MeV ( $J^\pi = 0^+$ ) and second 21.01 MeV ( $J^\pi = 0^-$ ) excited states [15]. The comparison of simulated and measured  $e^+e^-$  pair angular correlations in the  $E_{\text{sum}} \in [18, 22]$  MeV region is shown in Figure 0.1c.

In 2022, another anomaly was measured in the  ${}^{11}\text{B}(p, e^+e^-){}^{12}\text{C}$  process [16]. The  $E_p = 1388$  keV resonance was used to populate the 17.23 MeV excited state ( $J^\pi = 1^-$ ,  $T = 1$ ) with a large width  $\Gamma = 1.15$  MeV [17]. This state decays mainly through E1 transitions to the ground state  $J^\pi = 0^+$  and to the 4.44 MeV state  $J^\pi = 2^+$ . To compensate for energy losses in the target, five energies in the range  $E_p = 1.5\text{--}2.5$  MeV were used. The experimental angular correlation for the 17.23 MeV transition to the ground state is shown in Figure 0.1d.

Possible explanations of the anomaly include experimental effects, higher order processes in the Standard Model [18, 19] or even a protophobic fifth force mediated by a new 17 MeV boson X17 [20]. **Not sure if the introduction should be referenced since even though it is related, it is an independent theory developed only (?) to explain these measurements. Zhang and Miller: <https://www.sciencedirect.com/science/article/pii/S0370269321000010>**

### 0.1.2 Other Experiments

Since the ATOMKI measurements, several experiments have been initiated to attempt to replicate the results and search for the hypothetical X17 particle. The following experiments have already produced results. **Could cite the ATOMKI review paper here.**

#### Two-arm $e^+e^-$ spectrometer in Hanoi

The anomaly in  ${}^8\text{Be}$  has been observed with a high ( $> 4\sigma$  **That's all they write in their article.**) confidence by a team at the Hanoi University of Sciences for

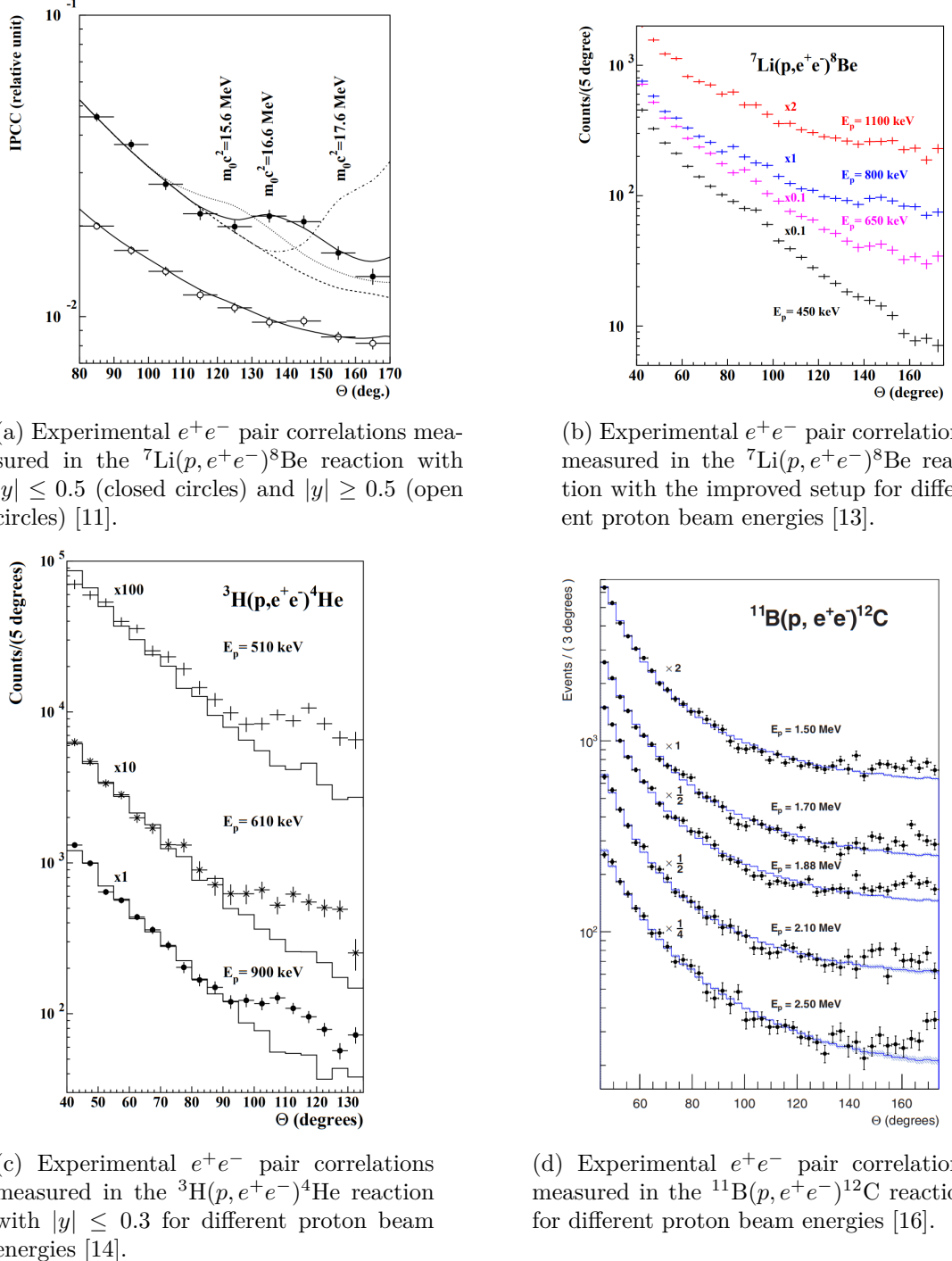


Figure 0.1: The ATOMKI anomalous IPC measured for different nuclei.

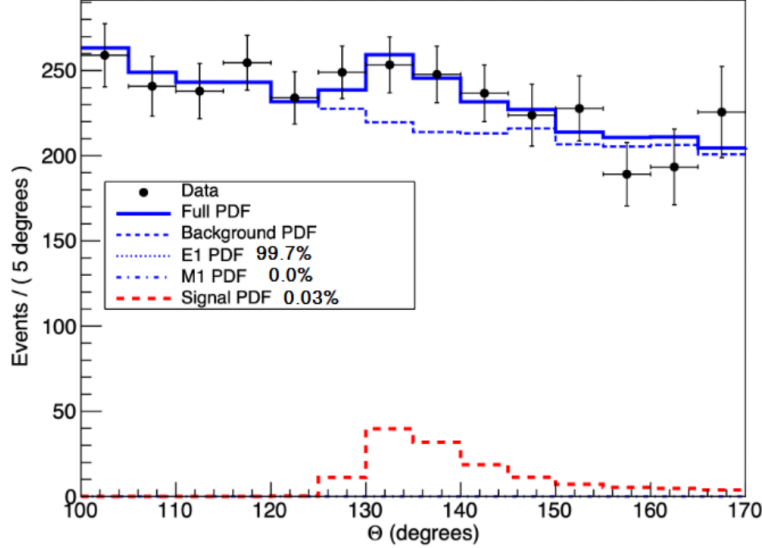


Figure 0.2: Results from the Hanoi spectrometer – angular  $e^+e^-$  pair correlations measured in the  ${}^7\text{Li}(p, e^+e^-){}^8\text{Be}$  reaction at  $E_p = 1225$  keV [21].

143  $E_p = 1225$  keV [21]. They built a two-arm spectrometer in collaboration with  
144 ATOMKI and calibrated it using the 17.6 MeV M1 transition. The results are  
145 shown in Figure 0.2.

#### 146 Collisions at Nuclotron in Dubna

147 At the Joint Institute for Nuclear Research in Dubna, signal in the form of en-  
148 hanced structures in the  $\gamma\gamma$  spectra at  $\sim 17$  and  $38$  MeV invariant masses for  
149  $p + \text{C}$ ,  $d + \text{C}$  and  $d + \text{Cu}$  reactions at momenta  $5.5$ ,  $2.75$ , and  $3.83$  GeV per nu-  
150 cleon [22]. Monte Carlo simulations support the conclusion that the signals are  
151 a consequence of a decay of unknown particles X17 and E38.

#### 152 The MEG II (Muon Electron Gamma) experiment

153 Experiments using the  ${}^7\text{Li}(p, e^+e^-){}^8\text{Be}$  reaction were carried out at the Paul  
154 Scherrer Institute with the MEG II superconducting solenoid spectrometer [23].  
155 Analysis of the data with  $E_p = 1080$  keV exciting both of the resonances (beam  
156 fully stopping in the target) found no significant evidence supporting the X17  
157 hypothesis, results are shown in Figure 0.3. An upper bound (at 90% confidence)  
158 on the X17-to- $\gamma$  branching ratio was set at  $1.2 \cdot 10^{-5}$  for the 18.15 MeV state  
159 (larger than the ratio  $5.8 \cdot 10^{-6}$  obtained by ATOMKI in 2016). Could add their  
160 90% C.L bounds figure also. Insufficient statistics – 6.2 % ( $1.5\sigma$ ) p-value.

## 161 0.2 X17 Project at IEAP CTU

162 The aim of the X17 project at the Van der Graaff facility of the Institute of Experi-  
163 mental and Applied Physics, Czech Technical University in Prague is to repeat the  
164 original ATOMKI experiments with  ${}^7\text{Li}$  and  ${}^3\text{H}$  targets using an independent  $e^+e^-$   
165 spectrometer. In order to effectively measure the anomaly, we need to reconstruct

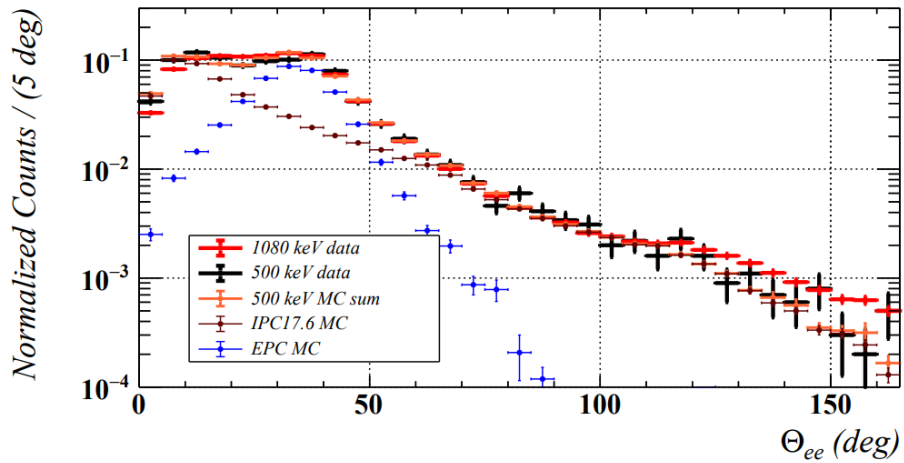


Figure 0.3: Results from the MEG II experiments – angular correlation of  $e^+e^-$  pairs with  $E_{\text{sum}} \in [16, 20]$  MeV measured in the  ${}^7\text{Li}(p, e^+e^-){}^8\text{Be}$  reaction with proton beam energies 500 and 1080 keV. The 500 keV dataset is fitted with Monte Carlo of both the IPC deexcitation and the EPC produced by gammas [23].

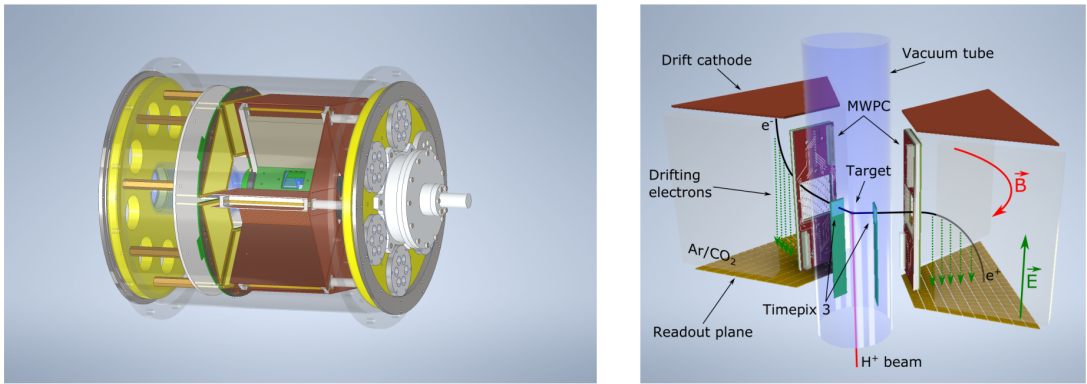


Figure 0.4: Schematics of the detector at the Van der Graaff facility at IEAP CTU.

166 both the energy and the angular correlation of the  $e^+e^-$  pairs. The spectrometer  
 167 will use three layers of detectors to achieve this – Timepix 3 (TPX3) silicon  
 168 pixel detector and Multi-Wire Proportional Chamber (MWPC) layers for the  
 169 angle reconstruction and a Time Projection Chamber (TPC) layer for the energy  
 170 reconstruction. The schematics of the prepared detector is in Figure 0.4 Spec-  
 171 trometer CAD drawing (coordinates here or next chapter?). Cite some VdG  
 172 paper, mention grant? Using [https://cernbox.cern.ch/pdf-viewer/public/  
 173 rf0oU1nqVLN3acZ/LuzH\\_submitted.pdf](https://cernbox.cern.ch/pdf-viewer/public/rf0oU1nqVLN3acZ/LuzH_submitted.pdf).

174 The energy of  $e^+e^-$  pair produced in the reaction is given by the energy  
 175 available  $E_r$  in the reaction and can be distributed between them arbitrarily.  
 176 Nonetheless in the decay of the hypothetical X17 particle, electron and positron  
 177 should have similar energy and we can therefore use a disparity cut  $|y| \leq 0.5$   
 178 for the disparity parameter (defined in Equation 0.1). Interesting events should  
 179 rarely have a particle with an energy below  $E_r/4$  (roughly 4 MeV). Electrons with  
 180 such low energies are scattered significantly by even a thin layer of relatively light

181 material, for this reason the TPX3 layer will be inside of the vacuum tube and  
182 the tube will have a thinned aluminum segment or Kapton™ windows.

183 TPX3 can measure (in each  $55 \times 55 \mu\text{m}$  pixel of its  $256 \times 256$  grid) time-of-arrival |  
184 (ToA) with 1.6 ns precision and time-over-threshold (ToT) which reflects the de-  
185 posited energy. This potentially allows 3D tracking if we increase the chip thick-  
186 ness at the cost of increased scattering. The layer can reconstruct the reaction  
187 vertex and the angular correlation with high precision.

188 The layer of MWPCs with sensitive area  $40 \times 38 \text{ mm}^2$  will be outside of  
189 the beam pipe. It will provide an extra point on the particle trajectory which can  
190 help with the estimation of the reaction vertex and improve the TPC performance  
191 by providing its entry point.

192 The TPCs, which are a subject of this theses, are in a magnetic field of per-  
193 manent magnets positioned between them and provide 3D track reconstruction  
194 and subsequent momentum and particle identification (its charge, or even type  
195 based on its stopping power). They avoid radiative losses thanks to the small  
196 interaction with the incident particle. For the readout, triple Gas Electron Mul-  
197 tiplier (GEM) will be used. The magnetic field layout in our TPCs is atypical –  
198 orthogonal to the electric field inside the chamber, this is why we call them Or-  
199 thogonal Fields TPC (OFTPC). Further details about our OFTPCs are provided  
200 in section 1.3.

# 1. Time Projection Chamber

201     Using (2010 – a little old) <https://cds.cern.ch/record/1302071/files/CERN-PH-EP-2010-047.pdf>  
203     A Time Projection Chamber (TPC) is a type of gaseous detector that uses  
204     the drift in an electric field of free charges (electrons and cations, also anions if  
205     attachment of electrons to the gas particles is considered) produced by an ionizing  
206     particle to reconstruct its 3D trajectory. When placed inside a magnetic field,  
207     the momentum of the incident particle can be inferred from the curvature of its  
208     trajectory. Particle identification is also possible using the ionization energy loss  
209     inside the TPC (see Figure 1.1). The detector used 80:20 Ar:CH<sub>4</sub> mixture at  
210     8.5 atm pressure.

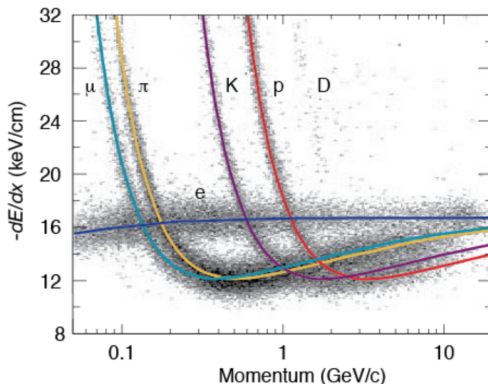


Figure 1.1: Particle identification in the PEP-4 TPC at SLAC based on the energy loss per distance  $\frac{dE}{dx}$  [24].

211     The original TPC used in the PEP-4 experiment at SLAC (Figure 1.2) was  
212     a  $2 \times 2$  m cylinder with a central cathode that produced a strong electric field,  
213     making the ionization electrons drift towards one of the bases. The readout  
214     consisted of MWPCs, where electrons are accelerated towards the anode wires  
215     enough to further ionize the gas and cause an avalanche.

216     When a charged particle crosses the volume of a TPC, it loses energy by excitation and ionization of the detector gas (how much – from  $dE/dx +$  density →  
217     footnote?). Most ionizing collision produce a single ionization electron, sometimes  
218     a few secondary electrons are produced close to the collision vertex. In rare cases,  
219     the ionization electron has energy large enough to create a measurable track, such  
220     an electron is called a  $\delta$ -electron (terminology, just like below – technically it's  
221     a (primary) ionization electron causing other (secondary) ionization). Penning  
222     transfer (collisions, light – factor 10 for gas gain in Ar/CO<sub>2</sub> viz PDG CERN)?  
223     CERES/NA45 – very inhomogeneous magnetic field

## 225     1.1 Charge transport in gases

### 226     1.1.1 Drift

227     Produced ionization electrons (terminology – called ionization electrons in the rest  
228     of the thesis, ionoelectrons?) are accelerated towards the readout by the electric

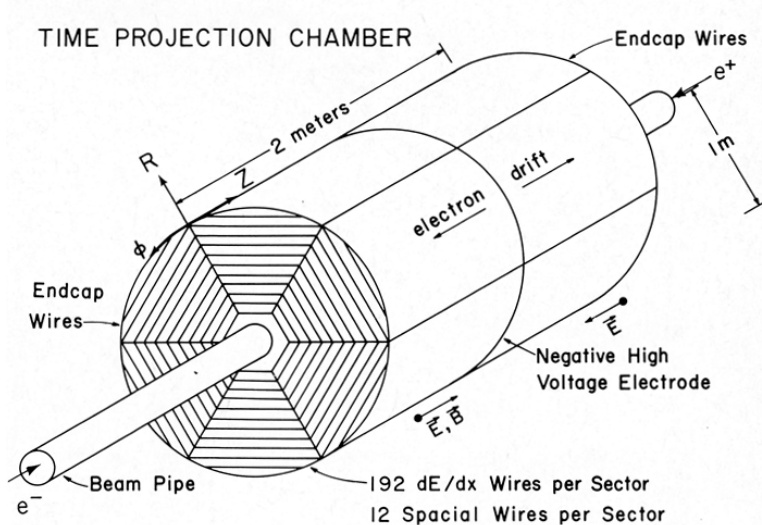


Figure 1.2: Schematic view of the PEP-4 TPC [25]. A charged particle produced in a collision in the beam pipe creates a spiral ionization track in the magnetic field. The central cathode then accelerates ionization electrons towards the endcap anode wires where they are multiplied and read out.

229 field inside the chamber. At the same time, they lose speed by colliding with  
 230 the gas particles, quickly reaching a constant (for a given field  $\mathbf{E}, \mathbf{B}$ ) mean drift  
 231 velocity. The electrons might be absorbed by electronegative impurities, such as  
 232 halides and oxygen.

233 In many gases (called "hot", e.g., Ar or  $\text{CH}_4$ ), the drift velocity (def? the  
 234 paragraph above not enough?) is much greater than that of their thermal motion  
 235 thanks to a high proportion of elastic collisions. On the other hand, "cold" gases  
 236 like  $\text{CO}_2$  have a higher proportion of inelastic collisions (e.g., thanks to the ex-  
 237 citation of rotational and vibrational states) and therefore much lower (value?  
 238 magnitude (implied)?) drift velocity.

239 The ions produced by the ionization lose a significant portion of their energy  
 240 during each collision since their mass is close to the mass of the gas particles (see  
 241 the source material – average energy loss during collision  $\Delta E = \frac{2m_i M}{(m_i + M)^2}$ , this way  
 242 it's more accurate). This, together with their large collision cross section, makes  
 243 their drift velocity much smaller and their energy is close to thermal. Since their  
 244 momenta aren't randomized to such an extent during collisions, their diffusion  
 245 is smaller (more in the sense of distribution of positions, could move this to the  
 246 diffusion subsection).

247 The drift is also influenced by the magnetic field. Langevin derived a good  
 248 approximation for the drift velocity vector:

$$\mathbf{v}_d = \left( \frac{\mathbf{E}}{\|\mathbf{E}\|} + \omega\tau \frac{\mathbf{E} \times \mathbf{B}}{\|\mathbf{E}\| \|\mathbf{B}\|} + \omega^2 \tau^2 \frac{\mathbf{E} \cdot \mathbf{B}}{\|\mathbf{E}\| \|\mathbf{B}\|} \cdot \frac{\mathbf{B}}{\|\mathbf{B}\|} \right) \frac{q\tau}{m(1 + \omega^2 \tau^2)} \|\mathbf{E}\|, \quad (1.1)$$

249 where  $q$  is the charge of the particle,  $m$  is its mass,  $\tau$  is the mean time between col-  
 250 lisions and  $\omega = \frac{q}{m} \|\mathbf{B}\|$  is the Larmor frequency. In a standard TPC,  $\mathbf{E}$  is nearly  
 251 parallel to  $\mathbf{B}$  and the influence of the magnetic field on the drift is minimal.  
 252 The drift of ions is only negligibly influenced by the magnetic field ( $\omega\tau \sim 10^{-4}$  is

253 small due to the low drift velocity – better because it takes  $\tau$  into account and  
 254 differs only by E/B ratio). Lorentz angle for orthogonal fields  $\tan \psi = -\omega\tau$  (de-  
 255 viation from electric field) – mention in the OFTPC section. Without magnetic  
 256 field, we can write

$$\mathbf{v}_d = \frac{q\tau}{m} \mathbf{E} = \mu \mathbf{E}, \quad (1.2)$$

257 where  $\mu$  is called charge mobility.

### 258 1.1.2 Diffusion

259 Due to collisions a cloud of electrons or ions originating from the same point will  
 260 show a Gaussian density distribution at time  $t$  while drifting in the electric field  
 261  $\mathbf{E} = (0, 0, E_z)$  along the  $z$ -coordinate (coordinates defined by the electric field):

$$\rho(x, y, z, t) = (4\pi Dt)^{-\frac{3}{2}} \exp\left(-\frac{x^2 + y^2 + (z - v_d t)^2}{4Dt}\right), \quad (1.3)$$

262 where the diffusion coefficient  $D$  can be expressed as

$$D = \frac{\lambda^2}{3\tau} = \frac{\lambda v_d}{3} = \frac{v_d^2 \tau}{3} = \frac{2\varepsilon\tau}{3m}, \quad (1.4)$$

263 where  $\lambda$  is the mean free path and  $\varepsilon$  the mean energy. The lateral diffusion width  
 264  $\sigma_x$  after a drift distance  $L$  can be expressed as

$$\sigma_x^2 = 2Dt = \frac{4\varepsilon L}{3qE}. \quad (1.5)$$

265 The minimal diffusion width is given by the lowest possible energy of the particles  
 266  $\varepsilon_{\text{th}} = \frac{3}{2}kT$  (corresponding to thermal motion):

$$\sigma_{x, \text{min}}^2 = \frac{2kTL}{qE}. \quad (1.6)$$

267 For electrons in "cold gases" (e.g., Ar/CO<sub>2</sub> mixture), the diffusion approaches  
 268 this limit up to a certain field intensity ( $\sim 100$  V/cm at 1 atm pressure)<sup>1</sup>. In  
 269 reality, the transversal diffusion of electrons can differ significantly from their  
 270 longitudinal diffusion and simulations are necessary to get a precise result.

271 In most TPCs, the transversal (but not the longitudinal) diffusion is reduced  
 272 by the magnetic field, since it is parallel to the electric field and curves the dif-  
 273 fusing electrons around their mean trajectory:

$$\frac{D_T(B)}{D_T(0)} = \frac{1}{C + \omega^2 \tau_2^2}, \quad (1.7)$$

274 where  $C$  and  $\tau_2$  are parameters dependent on the gas used. At low intensity of  
 275 the magnetic field, we can use an approximation  $C \approx 1$  and  $\tau_2 \approx \tau$ .

---

<sup>1</sup>For us  $\sigma_{x, \text{min}} = 0.45$  mm, quite close to the actual diffusion 0.5–0.7 mm – details of the calculation.

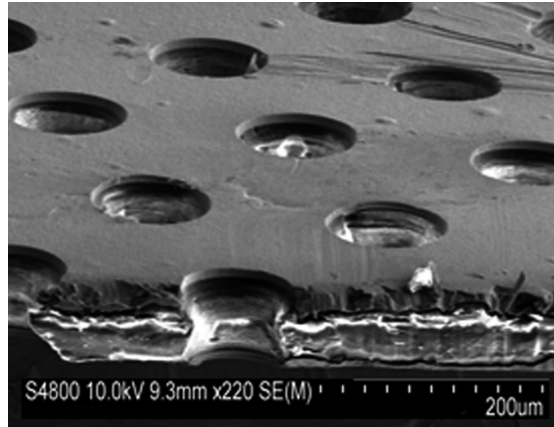


Figure 1.3: A scanning electron microscope image of a GEM foil [26].

## 276 1.2 Readout

### 277 1.2.1 Multi-Wire Proportional Chamber

278 In most (2010 – almost all) TPCs operated in experiments Multi-Wire Proportional Chamber (MWPC) (actually wire chamber – similar) was used for the readout. The electrons enter the chamber through a cathode grid and get accelerated in the strong electric field towards the thin anode wires and create a Townsend avalanche (ref), multiplying the signal. Alternating with field wires? That is the difference between MWPC and a drift chamber? The trajectory can be reconstructed using signal from each separate wire. Segmented cathode is also often used for the readout of produced cations. Gating grid (reduction of space charge effect, blocking backflow of ions?, closed for electrons  $B=0$ ,  $\Delta V$ , static mode (loss of 25% el.) x opening on trigger)? (gas amplification  $> 10000$  required for good SNR, 100-200 ns shaping time), figure – field (acts as a plane from far away and the field only gets strong enough for avalanches)?

### 290 1.2.2 Gas Electron Multiplier

291 A Gas Electron Multiplier (GEM) is a thin metal-coated polymer sheet with 292 a high density of small holes (Figure 1.3). The amplification is achieved by applying voltage on the metal layers, creating a strong electric field inside the holes 294 and causing avalanches (see Figure 1.4). Double or triple stack of GEMs is usually used to create a sufficient gain. From the last foil, the electrons drift to 296 a segmented anode where the signal is read. The backflow of cations is reduced 297 compared to MWPC. Typical parameters (vs thick GEM?).

### 298 1.2.3 Micromegas

299 In a MICRO-MEsh GAseous Structure (Micromegas) (in sources I viewed it is not 300 capitalized) electrons pass through a fine mesh (made out of very thin wires) into 301 the narrow amplification gap where they are multiplied in the high field and read 302 as signal on the segmented anode. Very high field ( $30-80 \text{ kV/cm}^2$ ) is necessary 303 to achieve sufficient gain. Cation backflow is heavily suppressed by the mesh.

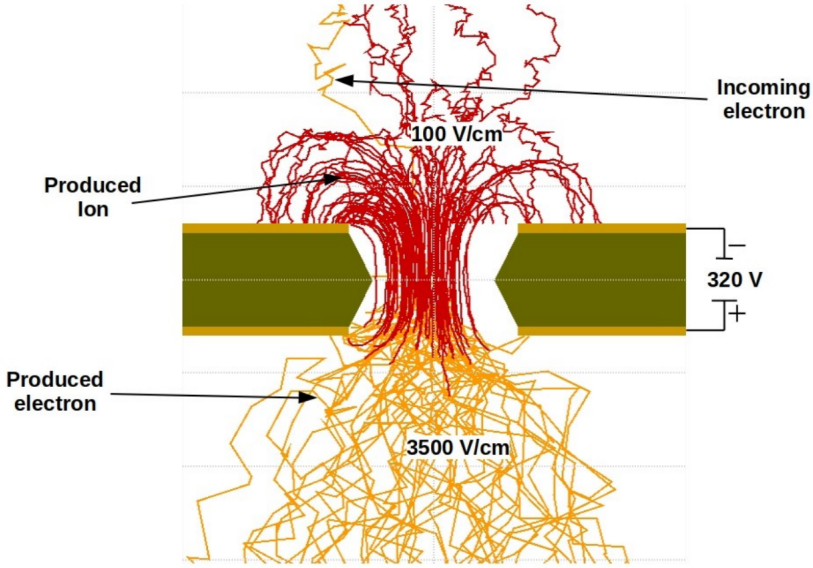


Figure 1.4: Garfield simulation of an avalanche in a GEM hole [27]. An incoming electron (orange) is accelerated in the strong electric field of the GEM and causes further ionization multiplying the number of free electrons (orange). Most of the produced cations (red) are captured by the GEM cathode.

#### 304 1.2.4 Parallel Plate Chamber

305 ... micowell? – these readouts and Micromegas are not used in our detector,  
 306 so maybe just mention them at the beginning of the readout section without  
 307 excessive detail (some subfigures showing how they look without describing each  
 308 too much)

### 309 1.3 Orthogonal Fields TPC at IEAP CTU

310 At IEAP CTU, we are going to use six identical atypical TPCs with inhomogeneous  
 311 toroidal magnetic field **orthogonal** to the electric field (**details below**),  
 312 hereafter referred to as Orthogonal Fields TPC (OFTPC). It has the shape of  
 313 isosceles trapezoidal prism 16 centimeters high with triple-GEM readout on one  
 314 of its bases. Dimensions of the OFTPC are discussed in detail in section 1.3.2  
 315 below. Throughout this thesis, we assume a uniform electric field along the  $z$  axis  
 316 with  $E_z = -400$  V/cm. Isn't the field affected by the MWPCs? Measured parti-  
 317 cles enter the OFTPC through a window after crossing the MWPC. Gas mixture  
 318 used in the detector (70/30) and its effect – some graph with the mixture. Add  
 319 a figure of the real TPC.

#### 320 1.3.1 Motivation and Associated Challenges

321 The reasons for the unusual field layout are mostly cost related:  
 322 a) we use permanent magnets instead of a solenoid and parallel fields are  
 323 difficult to accomplish this way,  
 324 b) granularity of the TPC readout is limited in order to fit one SAMPA/SRS  
 325 hybrid in each sector – parallel fields would bend the trajectories parallel

326 to the readout requiring more pads and different architecture.

327 In this thesis, we will show that such a setup can reach a similar energy resolution  
328 as common cylindrical TPCs while reducing the overall cost.

329 The layout introduces two complications to the track reconstruction – the  
330 trajectory in inhomogeneous field is not circular and the drift is distorted by the  
331 magnetic field as shown in the Equation 1.1(in our case  $\omega\tau \approx 0.08$  for 0.3 T  
332 assuming  $\mu \approx 0.25 \text{ T}^{-1}$ , varies inside the detector). We will deal with these  
333 effects in the upcoming chapters.

334 The diffusion in such setup is larger since parallel orientation reduces diffusion  
335 by curling the electrons in the  $x$ - $y$  direction (see Equation 1.7), but for our  
336 relatively weak magnetic field and short drift distance, the difference is negligible.

### 337 1.3.2 Coordinate Systems and Dimensions

338 In order to describe events in our detector, we use three distinct spaces: the de-  
339 tector space  $\mathcal{D}$ , the readout space  $\mathcal{R}$  and the pad space  $\mathcal{P}$  (different spaces that  
340 describe different things and each has their own coordinate system, so maybe  
341 rename the section somehow?). Each space is later used to represent ionization  
342 electrons at different stages of the detection process: their creation in the gas,  
343 their final position when hitting the readout plane, and finally their representation  
344 in the discrete pad space.

#### 345 Detector Space

346 The detector space  $\mathcal{D}$  represents the physical space of our detector. We de-  
347 scribe it using Cartesian coordinates  $(x, y, z)$ . The  $z$ -axis is the detector's axis of  
348 symmetry, with its negative direction aligned with the proton beam. The origin  
349  $(0, 0, 0)$  is located at the center of the irradiated target. The positive  $x$ -axis passes  
350 through the center of one the OFTPCs along the intersection of its two planes  
351 of symmetry. The  $y$ -axis is then chosen to maintain a right-handed coordinate  
352 system.

353 Since the detector has a hexagonal symmetry, we use only one of its sectors  
354 in this work – the first sector  $\mathcal{D}_1 \subset \mathcal{D}$  which is defined by the condition:

$$(x, y, z) \in \mathcal{D}_1 \Leftrightarrow |y| \leq x \tan \frac{\pi}{6}. \quad (1.8)$$

355 Simulations in this sector can be applied to all sectors by rotating the coordinates  
356 accordingly. The volume of the OFTPC in this sector, which has the shape of  
357 a trapezoidal prism, has these boundaries:

$$x \in [x_{\min}, x_{\max}] = [6.51, 14.61] \text{ cm}, \quad (1.9)$$

$$z \in [z_{\min}, z_{\max}] = [-8, 8] \text{ cm}, \quad (1.10)$$

$$y_{\max}(x_{\min}) = -y_{\min}(x_{\min}) = 2.75 \text{ cm}, \quad (1.11)$$

$$y_{\max}(x_{\max}) = -y_{\min}(x_{\max}) = 7.45 \text{ cm}, \quad (1.12)$$

358 where  $y_{\max}(x)$  is the maximal value of the  $y$ -coordinate for a given  $x$ . The read-  
359 out is located at  $z = 8$  cm; for some purposes, we also define the distance to  
360 the readout  $d_r = 8$  cm –  $z$  as an alternative to the  $z$ -coordinate. Keeping this  
361 paragraph as it is because the OFTPC volume is distinct from the first sector

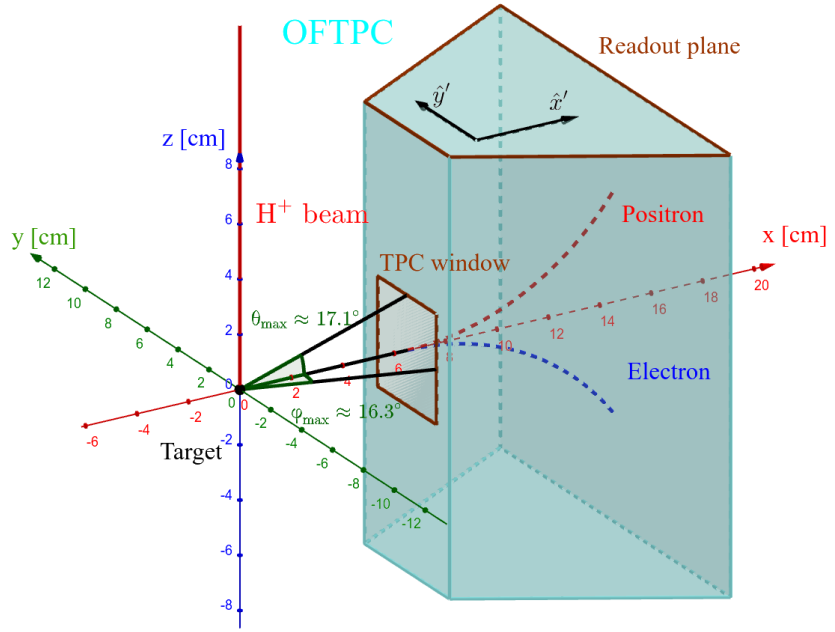


Figure 1.5: Schematics of the first sector OFTPC with detector space coordinates.

362 and some parts of this thesis use the space beyond this volume. The OFTPC  
 363 window has width 3.8 cm and height 4.0 cm.

364 We also use spherical coordinates  $(r, \theta, \varphi)$  with the elevation angle  $\theta$  measured  
 365 relative to the  $xy$  plane. Angles  $\theta$  and  $\varphi$  are useful when describing the direction  
 366 of  $e^+/e^-$  tracks. Their maximal values considered for the initial direction in  
 367 simulations are  $\theta_{\max} \approx 17.1^\circ$  and  $\varphi_{\max} \approx 16.3^\circ$  as shown in Figure 1.5.

### 368    Readout Space

369 The readout space  $\mathcal{R}$  represents the drift time and final positions of ionization  
 370 electrons as measured by an ideal continuous readout. We describe it using  
 371 coordinates  $(x', y', t)$ , where  $x'$  and  $y'$  correspond to the detector coordinates at  
 372 the readout plane ( $z = 8$  cm).

373 Currently not entirely sure how to put this into a figure since only  $x'$  and  
 374  $y'$  correspond to the detector coordinates, **it will make more sense when**  
 375 **visualizing the map**. The drift time  $t$  is approximately proportional to  $d_r$ .

### 376    Pad Space

377 The pad space  $\mathcal{P}$  represents the time bin and pad number of ionization electrons  
 378 as measured by an ideal discrete readout:

$$\mathcal{P} = \{(n_{\text{pad}}, n_t) \in \mathbb{N}^2 \mid n_{\text{pad}} \leq 128\}. \quad (1.13)$$

379 **Rewrite to reflect this:** Technically both values can be zero as defined in  
 380 the code (max channel 127). It is not really a subspace of  $\mathcal{R}$  but there is a  
 381 mapping from  $\mathcal{R}$  to  $\mathcal{P}$ . It is a discretization of a part of  $\mathcal{R}$ , the mapping can be  
 382 adjusted depending on the simulation. If we assume uniform electric field there  
 383 will be gaps, we don't use gaps in the reconstruction since the electrons should  
 384 be pulled towards the pads.

385 The readout of the OFTPC will consist ([is the design final?](#)) of 128 rectangular  
 386 pads arranged in a staggered pattern. Parameters of the pad layout are shown  
 387 in Figure 1.6. The bottom left corner of  $n$ -th pad has coordinates  $(x_{1,n}, y_{1,n})$ ,  
 388 the top right  $(x_{2,n}, y_{2,n})$  and its center has coordinates  $(x_{c,n}, y_{c,n})$ . The gap  
 389 between neighboring pads is  $g = 0.08$  cm. Time will be read out in discrete bins  
 390 of size  $t_{\text{bin}} = 100$  ns ([details?](#)). Could also describe pad-related functions.

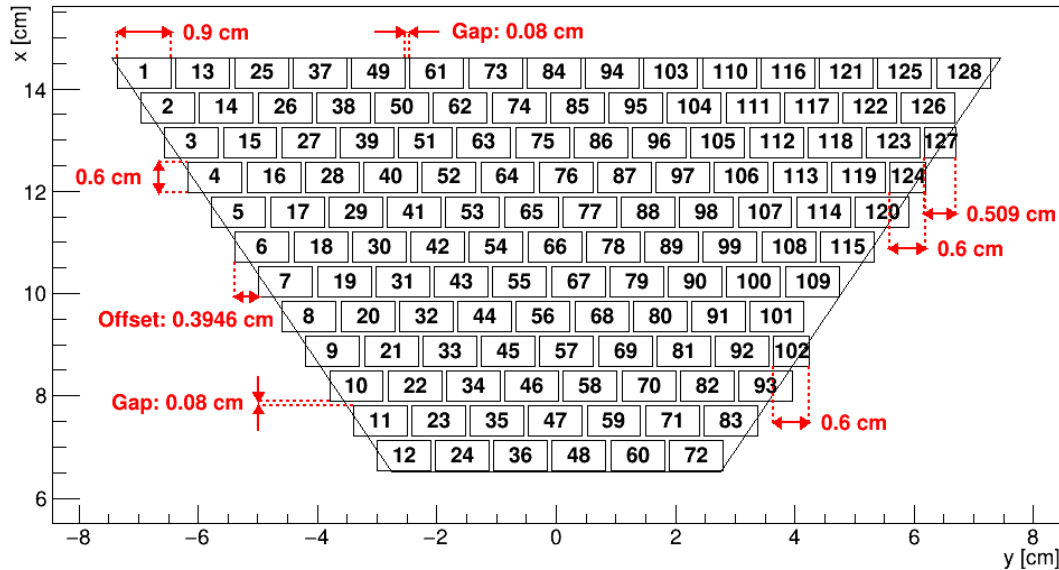


Figure 1.6: Pad layout of the OFTPC and its parameters. Pads 102, 124 and 127 are irregular, the rest has the same dimensions.

### 391 1.3.3 Magnetic Field Simulation

392 The magnetic field inside our detector is produced by six permanent magnets. It  
 393 was simulated using Ansys Maxwell ([citation](#)) which gives us values on a regular  
 394 grid. [More details, vacuum tube, magnets \(homogeneous?, density?\)](#). Visualiza-  
 395 tion of the magnetic field is shown in Figure 1.7. Whenever we need to work with  
 396 values outside this grid, we use trilinear interpolation described below.

### 397 Trilinear Interpolation

398 Trilinear interpolation is a 3D generalization of linear interpolation<sup>2</sup>. It can be  
 399 used to interpolate a function whose values are known on a regular grid with  
 400 rectangular prism cells. We use this simple method for interpolating the magnetic  
 401 field, and it is later used in Section 3.2.1 to interpolate the Ionization Electron  
 402 Map, a key component of our track reconstruction algorithm. In both cases, we  
 403 use a regular cubic grid ([apparently it is also called a Cartesian grid](#)).

404 Let us consider a cell of our regular grid (a cube) with an edge of length  $a$   
 405 containing the point  $\mathbf{C} = (x, y, z)$  where we want to interpolate a function  
 406  $f: \mathbb{R}^3 \rightarrow \mathbb{R}$ . We know the values of this function at the vertices of the cell  $\mathbf{C}_{ijk} =$   
 407  $= (x_0 + ia, y_0 + ja, z_0 + ka)$ , where  $\mathbf{C}_{000} = (x_0, y_0, z_0)$  is the origin of the cell ([is](#)

---

<sup>2</sup>Linear interpolation in point  $x \in (x_1, x_2)$  of a function  $f: \mathbb{R} \rightarrow \mathbb{R}$  known in points  $x_1 < x_2$  is the convex combination  $\hat{f}(x) = (1 - x_d)f(x_1) + x_d f(x_2)$ , where  $x_d = \frac{x - x_1}{x_2 - x_1} \in (0, 1)$ .

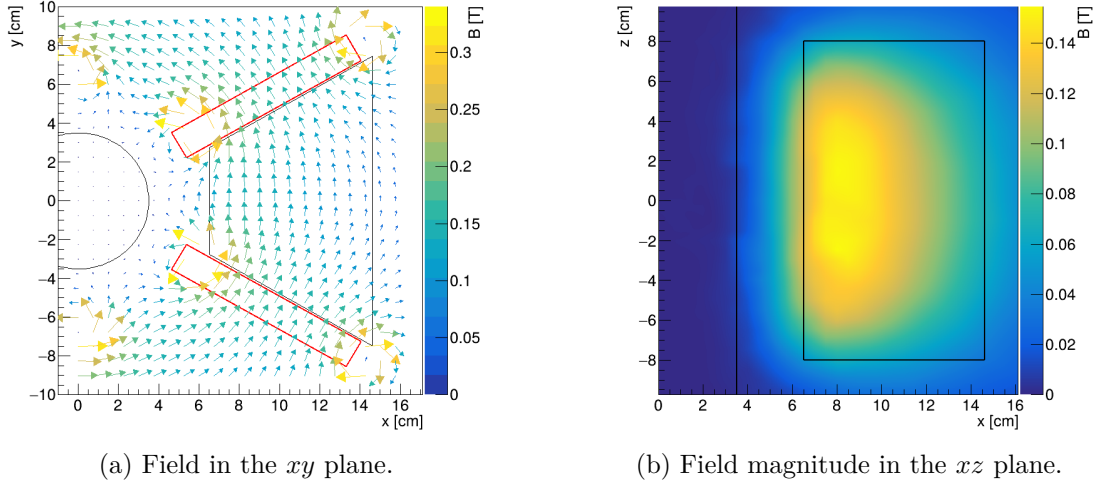
(a) Field in the  $xy$  plane.(b) Field magnitude in the  $xz$  plane.

Figure 1.7: Magnetic field simulation results. The OFTPC volume and the vacuum tube are marked with black lines, the magnets are marked with red lines. **The coordinates of the magnets from the CAD drawing seem to be 9/10 of the ones from the magnetic simulation (confirm and fix).**

408 that clear?), and  $i, j, k \in \{0, 1\}$  are indices. We also define the points  $\mathbf{C}_{ij} =$   
 409  $= (x, y_0 + ia, z_0 + ja)$  and  $\mathbf{C}_i = (x, y, z_0 + ia)$ . Then the interpolated value  $\hat{f}(\mathbf{C})$   
 410 can be calculated as a composition of three linear interpolations (see Figure 1.8):

$$\hat{f}(\mathbf{C}_{ij}) = (1 - x_d) f(\mathbf{C}_{0ij}) + x_d f(\mathbf{C}_{1ij}), \quad (1.14)$$

$$\hat{f}(\mathbf{C}_i) = (1 - y_d) \hat{f}(\mathbf{C}_{0i}) + y_d \hat{f}(\mathbf{C}_{1i}), \quad (1.15)$$

$$\hat{f}(\mathbf{C}) = (1 - z_d) \hat{f}(\mathbf{C}_0) + z_d \hat{f}(\mathbf{C}_1), \quad (1.16)$$

411 where  $x_d$ ,  $y_d$ , and  $z_d$  are given as follows:

$$x_d = \frac{x - x_0}{a}, \quad y_d = \frac{y - y_0}{a}, \quad z_d = \frac{z - z_0}{a}. \quad (1.17)$$

412 We can also write

$$\hat{f}(\mathbf{C}) = \sum_{i,j,k \in \{0,1\}} t_x^i t_y^j t_z^k f(\mathbf{C}_{ijk}), \quad (1.18)$$

$$t_\alpha \stackrel{\text{def}}{=} \begin{pmatrix} t_\alpha^0 \\ t_\alpha^1 \end{pmatrix} = \begin{pmatrix} 1 - \alpha_d \\ \alpha_d \end{pmatrix}, \quad (1.19)$$

413 where  $\alpha \in \{x, y, z\}$  is an index. This gives a nice geometric interpretation to the  
 414 trilinear interpolation as shown in Figure 1.9. From this form and the figure, it  
 415 is apparent that the final interpolated value does not depend on the order of axes  
 416 along which we perform linear interpolations (see Figure 1.8). Furthermore, we  
 417 can write  $\hat{f}(\mathbf{C})$  as a polynomial:

$$\hat{f}(\mathbf{C}) = \sum_{\alpha, \beta, \gamma \in \{0,1\}} \sum_{i=0}^{\alpha} \sum_{j=0}^{\beta} \sum_{k=0}^{\gamma} (-1)^{(\alpha-i) + (\beta-j) + (\gamma-k)} f(\mathbf{C}_{ijk}) x_d^\alpha y_d^\beta z_d^\gamma. \quad (1.20)$$

418 We take advantage of this form when generalizing trilinear interpolation to irregular  
 419 grid in section 3.2.2.

420 Maybe a citation here, although I am not sure it is necessary since it could  
 421 be considered common knowledge. The last two equations are my own (but I'm  
 422 not sure that's worth mentioning unless there's a citation).

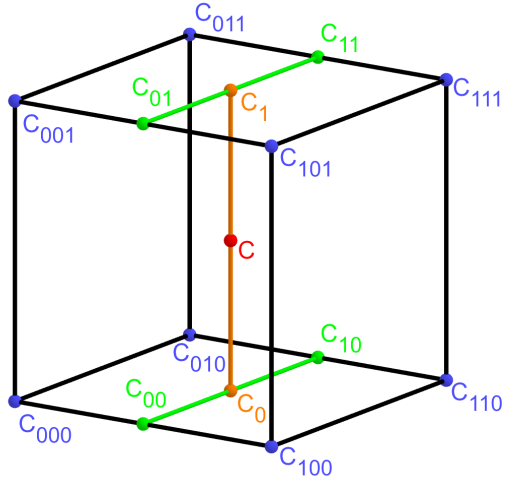


Figure 1.8: Visualization of trilinear interpolation as a composition of linear interpolations (inspired by [28]). We want to interpolate the value in the red point  $\mathbf{C}$ . First we interpolate between the four pairs of blue points sharing the last two indices along the  $x$ -axis (Eq. 1.14), then between the two pairs of the resulting green points along the  $y$ -axis (Eq. 1.15) and finally between the two resulting orange points along the  $z$ -axis to get the final red value (Eq. 1.16).

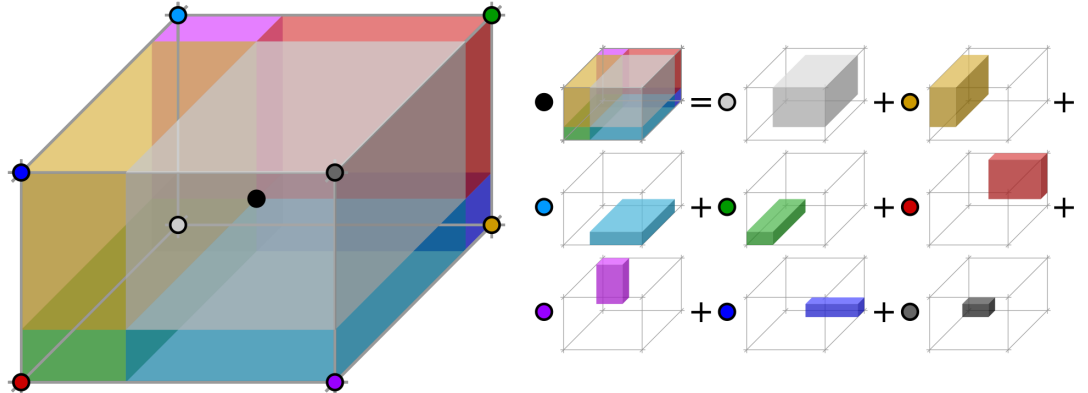


Figure 1.9: Geometric interpretation of trilinear interpolation as expressed in Equation 1.18. The colored dots represent the values in given points and the colored boxes represent the volume in the opposite corner by which the corresponding values are multiplied. The black dot represents the interpolated value which is multiplied by the entire volume [29].

## 2. Track Simulation

In order to develop and test the reconstruction algorithm, electron and positron tracks are simulated inside the first detector sector  $\mathcal{D}_1$  (see Section 1.3.2) with different initial parameters (origin, initial direction and kinetic energy). Two approaches are currently used to simulate tracks, each of them for different purpose.

The **Microscopic Simulation** uses the Garfield++ toolkit [1]. Within this toolkit:

- a) Magboltz, since it is mentioned later
- b) the High Energy Electro-Dynamics (HEED) program [30] is used to simulate the primary particle,
- c) the class *AvalancheMicroscopic* to simulate the drift of secondary electrons created by ionization in the gas.

This is the most precise and time-consuming simulation used; our current goal is to be able to successfully reconstruct its results and determine our best-case energy resolution.

The **Runge-Kutta Simulation** uses the 4th order Runge-Kutta numerical integration (add citation for Runge-Kutta) to simulate the trajectory of the primary particle in the electromagnetic field inside the detector. It is relatively fast since it does not simulate the secondary particles. It is used as part of our reconstruction algorithm and for testing some parts of the reconstruction.

All of these simulations require the knowledge of the electromagnetic field (both **E** and **B**) inside the detector. A uniform electric field of  $400 \text{ V}\cdot\text{cm}^{-1}$  is assumed. The magnetic field was simulated in Maxwell (see Section 1.3.3). add citation

Single track in positive x direction or initial parameter randomization. Importance of gas composition, used gas compositions.

### 2.1 Microscopic Simulation

The microscopic simulation, the most detailed simulation used in this work, is performed using the Garfield++ toolkit [1].

The electron transport properties are simulated using the program Magboltz (add citation), (details?). Two different gas mixtures were compared – 90:10 and 70:30 Ar:CO<sub>2</sub>. The second mixture will be used in our detector (this was probably known a priori, but the first tests that I started with used 90/10, so maybe just note that the results justify the fact so far). The temperature is set to 20 °C, the pressure is atmospheric.

The primary track is simulated using the program HEED, which is an implementation of the photo-absorption ionization model [30] (see the reference, moved it to the end of sentence). This program provides the parameters of ionizing collisions. HEED can also be used to simulate the transport of delta electrons; we do not account for these in the current simulation (but plan to include them in the future – maybe mention only in the conclusion/future section). The photons created in the atomic relaxation cascade (fluorescence reabsorption, related to the spread of avalanches in GM det.?) are also not simulated.

466 Finally, we use the microscopic tracking provided by the class *AvalancheMicroscopic*  
 467 in Garfield++ to simulate the drift of the ionization electrons. Each  
 468 electron is followed from collision to collision using the equation of motion and  
 469 the collision rates calculated by Magboltz.

470 Add more detailed and better description of HEED, and microscopic tracking  
 471 (each their own subsection?). Could also mention Monte Carlo (requires gas file  
 472 generation - Magboltz) and Runge-Kutta simulation implemented in Garfield,  
 473 why we don't use them (another subsection? rename the section to Garfield++  
 474 simulation and mention all relevant parts?).

### 475 2.1.1 First testing track

476 The first electron track simulated for testing purposes was chosen to have a special  
 477 set of parameters:

- 478 • the starting point of the track is the origin of the coordinate system,
- 479 • the initial direction is along the positive  $x$ -axis,
- 480 • the momentum is 8 MeV/c (the kinetic energy is 7.505 MeV).

481 Such a track moves in the XZ plane in the toroidal magnetic field of the detector,  
 482 because the particle's velocity vector is always perpendicular to the field. At first,  
 483 we simulated such a track in 90:10 Ar:CO<sub>2</sub> gas mixture, later we added a simu-  
 484 lation in 70:30 Ar:CO<sub>2</sub>, which we plan to use in our detector. The comparison of  
 485 both simulations is in Figure 2.1.

### 486 2.1.2 Grid-like testing sample

487 In order to test all steps of the reconstruction, a sample of tracks with a grid-like  
 488 distribution of parameters was generated on MetaCentrum. Five sets of 9702  
 489 tracks were generated with every combination of these parameters:

- 490 • electron and positron tracks,
- 491 • 11 different kinetic energies  $E_{\text{kin}} \in [3, 13]$  MeV,
- 492 • 21 different azimuth angles  $\varphi \in [-16.3^\circ, 16.3^\circ]$  and
- 493 • 21 different elevation angles  $\theta \in [-17.1^\circ, 17.1^\circ]$ .

494 A visualization of a set of  $e^+/e^-$  tracks with the same kinetic energy is shown  
 495 in Figure 2.2 (plotting actual HEED tracks using ROOT should be also possible  
 496 (but hard to make look good?)). In the 70:30 Ar:CO<sub>2</sub> atmosphere, each track  
 497 takes 5-30 CPU hours to simulate. Every tenth point on the drift line was stored,  
 498 the whole sample has 3.1 terabytes (or 1.4 gigabytes without drift lines).

## 499 2.2 Runge-Kutta Simulation

500 The Runge-Kutta simulation in this work uses the Runge-Kutta 4th order (RK4)  
 501 method to numerically integrate the equation of motion of a relativistic charged  
 502 particle in an electromagnetic field. Given a system of first order differential  
 503 equations

$$\frac{dy}{dt} = \mathbf{f}(t, \mathbf{y}(t)) \quad (2.1)$$

504 with an initial condition

$$\mathbf{y}(t_0) = \mathbf{y}_0, \quad (2.2)$$

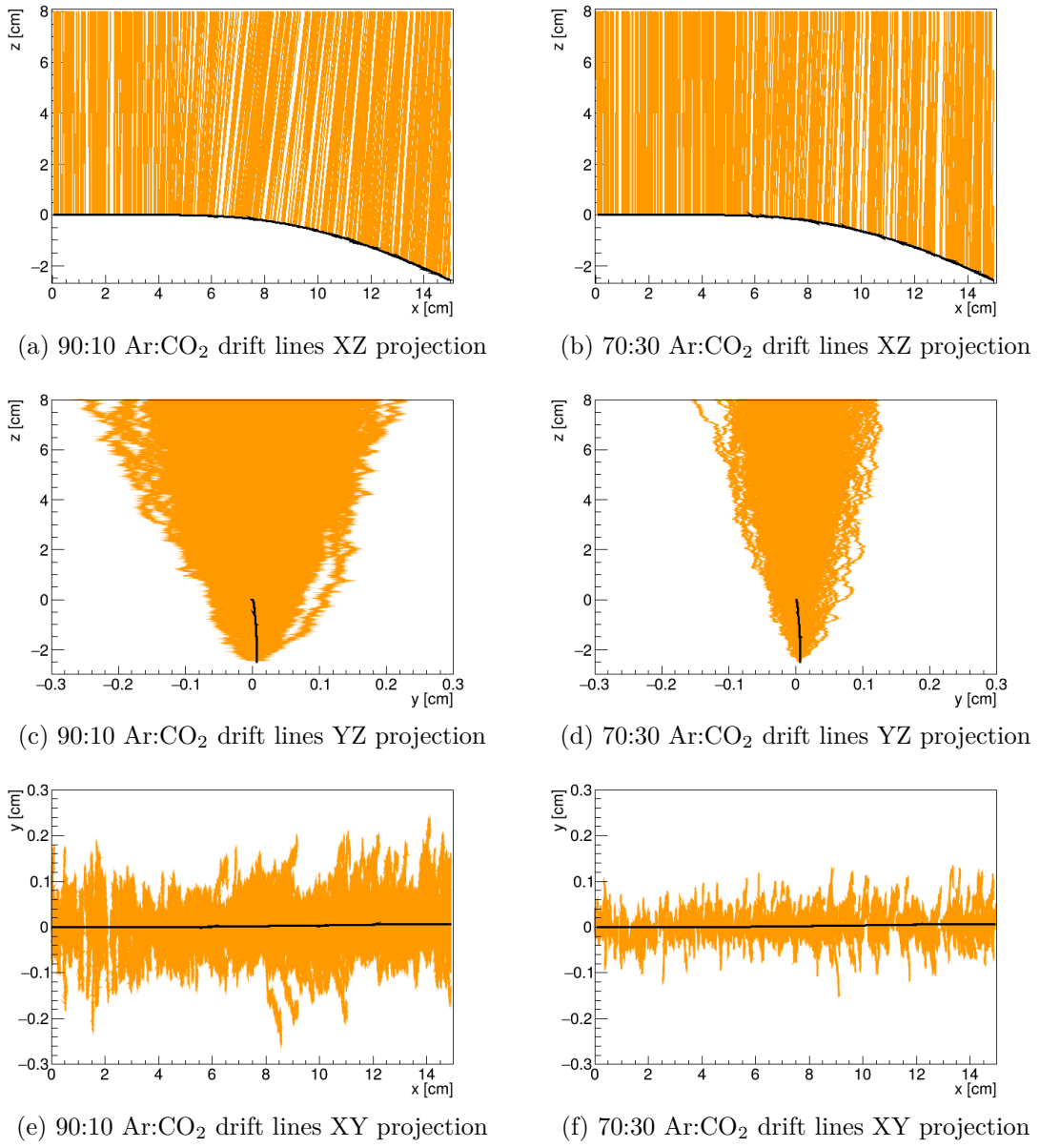


Figure 2.1: Comparison of drift lines for two different gas mixtures 90:10 and 70:30 Ar:CO<sub>2</sub>. The electron track is marked in black, the drift lines of the ionization electrons are marked in orange. In this example, we assume a larger OFTPC volume with readout at  $z = 8$  cm.

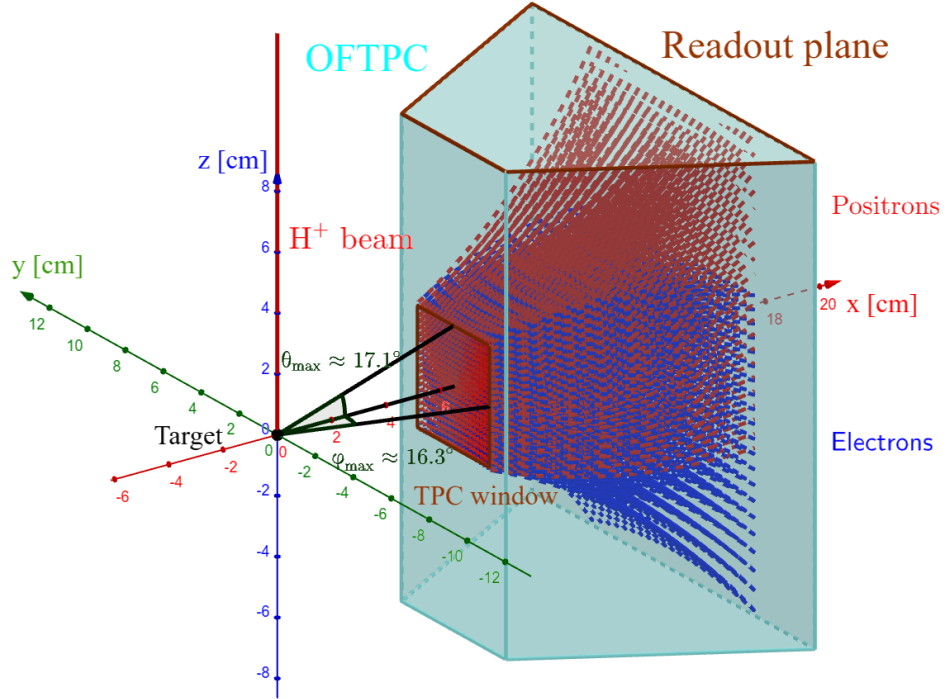


Figure 2.2: A visualization of a set of tracks from the grid-like testing sample with the same kinetic energy.

505 we iteratively compute the estimate  $\mathbf{y}_n = \mathbf{y}(t_n) = \mathbf{y}(t_0 + nh)$  as follows (citation?  
 506 common knowledge?):

$$\mathbf{k}_1 = \mathbf{f}(t_n, \mathbf{y}_n), \quad (2.3)$$

$$\mathbf{k}_2 = \mathbf{f}\left(t_n + \frac{h}{2}, \mathbf{y}_n + \frac{h\mathbf{k}_1}{2}\right), \quad (2.4)$$

$$\mathbf{k}_3 = \mathbf{f}\left(t_n + \frac{h}{2}, \mathbf{y}_n + \frac{h\mathbf{k}_2}{2}\right), \quad (2.5)$$

$$\mathbf{k}_4 = \mathbf{f}(t_n + h, \mathbf{y}_n + h\mathbf{k}_3), \quad (2.6)$$

507

$$\mathbf{y}_{n+1} = \mathbf{y}_n + \frac{1}{6}(\mathbf{k}_1 + 2\mathbf{k}_2 + 2\mathbf{k}_3 + \mathbf{k}_4). \quad (2.7)$$

508 Alternate forms (infinitely many) possible, accuracy vs computational cost. Runge-  
 509 Kutta-Fehlberg with adaptive step size also possible, can potentially save some  
 510 computation time especially in rapidly changing field (so maybe not in this case).

511 In our case, we want to integrate the equation of motion, given by the rela-  
 512 tivistic Lorentz force:

$$F_L^\mu = m \frac{du^\mu}{d\tau} = q F^{\mu\nu} u_\nu, \quad (2.8)$$

513 where the Einstein summation convention is used,  $m$  is the mass of the particle,  
 514  $q$  is its charge,  $u^\mu$  is its four-velocity,  $\tau$  is the proper time (i.e., time in the particle's  
 515 frame of reference) and  $F^{\mu\nu}$  is the electromagnetic tensor at given coordinates  $x^\mu$   
 516 (we consider it to be time-independent in our detector). Given the electric  $\mathbf{E} =$   
 517  $= (E_x, E_y, E_z)$  and the magnetic field  $\mathbf{B} = (B_x, B_y, B_z)$  and using the metric

518 signature  $(+, -, -, -)$ , the equation expands to

$$\frac{d}{d\tau} \begin{pmatrix} \gamma c \\ \gamma v_x \\ \gamma v_y \\ \gamma v_z \end{pmatrix} = \frac{q}{m} \begin{pmatrix} 0 & -\frac{E_x}{c} & -\frac{E_y}{c} & -\frac{E_z}{c} \\ \frac{E_x}{c} & 0 & -B_z & B_y \\ \frac{E_y}{c} & B_z & 0 & -B_x \\ \frac{E_z}{c} & -B_y & B_x & 0 \end{pmatrix} \begin{pmatrix} \gamma c \\ \gamma v_x \\ \gamma v_y \\ \gamma v_z \end{pmatrix}, \quad (2.9)$$

519 where  $c$  is the speed of light in vacuum,  $\mathbf{v} = (v_x, v_y, v_z)$  is the particle's velocity  
 520 and  $\gamma = (1 - \frac{v^2}{c^2})^{-\frac{1}{2}}$  is the Lorentz factor (wrong magnetic field sign in the  
 521 implementation???). Together with the equation

$$\frac{d}{d\tau} \begin{pmatrix} ct \\ x \\ y \\ z \end{pmatrix} = \begin{pmatrix} \gamma c \\ \gamma v_x \\ \gamma v_y \\ \gamma v_z \end{pmatrix} = u^\mu, \quad (2.10)$$

522 we get a system of eight first order differential equations for  $x^\mu$  and  $u^\mu$ , which  
 523 we can integrate using the Runge-Kutta method described above. As a result of  
 524 this integration, we get the position  $\mathbf{x}(\tau_n)$ , the velocity  $\mathbf{v}(\tau_n)$  and the detector  
 525 time  $t(\tau_n)$  for every proper time  $\tau_n = n\tau_{\text{step}}$ . Integrating using the proper time  
 526 means that the step size in  $t$  gets larger by the gamma factor  $\frac{dt}{d\tau} = \gamma$  (maybe  
 527 change it and integrate the detector time or adjust the step size accordingly). The  
 528 only difference is in the step size (because  $t$  gets also calculated as it is among the  
 529 8 variables). It might be even better to adjust the step size using approx-  
 530 imate distance traveled. As initial conditions, we use the origin of the track  
 531 ( $x_0, y_0, z_0$ ), the initial velocity direction vector  $\mathbf{n} = (\cos \varphi \cos \theta, \sin \varphi \cos \theta, \sin \theta)$   
 532 and the kinetic energy  $E_{\text{kin}}$  (initial parameters of the simulation (fit is in chap-  
 533 ter 4)), we then compute  $\gamma$  and  $\|\mathbf{v}\|$ :

$$\gamma = 1 + \frac{E_{\text{kin}}}{E_0}, \quad (2.11)$$

$$\|\mathbf{v}\| = c\sqrt{1 - \gamma^{-2}}. \quad (2.12)$$

### 534 2.2.1 Testing sample

535 Example of RK simulation – first testing track, randomized sample of 100000  
 536 tracks (could also move them to circle 3D fit).

537 In order to test the simulation and reconstruction, a sample of 100 000 tracks  
 538 with randomized parameters was generated:

- 539 • the Runge-Kutta step was set to 0.1 ns (proper time, which wouldn't be a  
 540 problem but this way the "spatial" step depends on energy),
- 541 • the kinetic energy of the particle  $E_{\text{kin}} \in [4, 12]$  MeV,
- 542 • the starting point of the track is a random point in the OFTPC window,
- 543 • the initial direction is given by the line connecting a random point on  
 544 the target<sup>1</sup> (a disc with 1 mm radius in the YZ plane).

---

<sup>1</sup>To generate a random point on the target, we generate a random angle  $\alpha$  and a random square of the distance from origin  $r^2$  to get a uniform distribution.

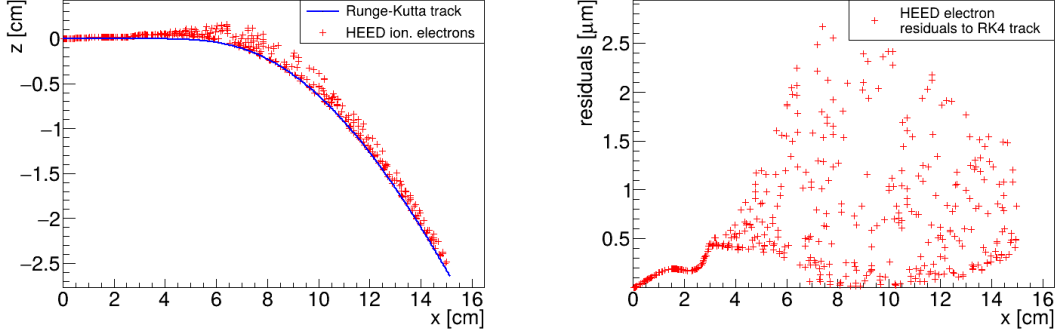


Figure 2.3: A comparison of the HEED track from the microscopic simulation in Section 2.1.1 with a Runge-Kutta track with the same initial parameters and  $\tau_{\text{step}} = 0.1 \text{ ps}$  (reducing the step further doesn't make a visible difference). In the view of the tracks on the left, the distance of the HEED ionization electrons from the RK4 track is exaggerated 1000 $\times$ . On the right, the dependence of the HEED electrons residuals (i.e., their shortest distance to the RK4 track) on their  $z$ -coordinate is shown. **The images look the same even for 100,000x smaller step, so the residuals are a result of something that HEED does.**

When exaggerating, the HEED ionization electrons are moved away along the shortest line connecting them to the RK4 track. The computation of this distance is described in Section 4.3.

545 Since the Runge-Kutta simulation is quite fast<sup>2</sup>, it can be run locally on any  
 546 computer. **Add a figure with simulated tracks (sample).** An example Runge-  
 547 Kutta track is compared with the corresponding microscopic track in Figure 2.3.

---

<sup>2</sup>One track with  $\tau_{\text{step}} = 0.1 \text{ ps}$  takes less than one millisecond to simulate.

### 548 3. Track Reconstruction

549 As the first step of the reconstruction algorithm, we reconstruct the track of  
550 a primary particle – either an electron or a positron. Then, using this information,  
551 we determine the energy of the particle (Section 4).

552 The **Reconstruction Assuming Steady Drift** uses the standard TPC ap-  
553 proach. With parallel fields, the drift inside a uniform electric field remains  
554 undistorted (as shown in Equation 1.1). Therefore, we only need to reconstruct  
555 the  $z$ -coordinate from the drift time using the known drift velocity. We also  
556 assume that the readout coordinates ( $x'$ ,  $y'$ ,  $t$ ) are known exactly, neglecting  
557 the pads and time binning.

558 Reconstruction using an **Ionization Electron Map** (from now on referred  
559 to as *the map*) uses a simulation of the drift of secondary (ionization) electrons  
560 within the detector volume. This simulation can then be used to interpolate  
561 the initial position of the secondary electrons. In the first iteration of this method  
562 the readout is assumed to be continuous.

563 We present two algorithms using the map for reconstruction. The first one uses  
564 a gradient descent algorithm along with trilinear interpolation (see Section 1.3.3)  
565 of the map. The second method uses interpolation on the irregular inverse grid  
566 with a polynomial.

567 The **Discrete Reconstruction** uses the map; instead of reconstructing the ex-  
568 act position of each electron, we reconstruct the center of each hit pad together  
569 with the time corresponding to the midpoint of the time bin. The electron count  
570 in each TPC bin (consisting of the pad and the time bin) serves as an idealized  
571 collected charge, which is then used as a weight in the energy reconstruction fit.

#### 572 3.1 Reconstruction Assuming Steady Drift

573 As the first step, we tried to reconstruct a simulated electron track with a special  
574 set of initial parameters, described in detail in Section 2.1.1. The starting point  
575 is given by the origin of our coordinate system and its initial direction is given by  
576 the positive  $x$ -axis. This means the magnetic field of our detector is perpendicular  
577 to the momentum of the particle at all times, and we can reduce the problem to  
578 two-dimensional space.

579 For the reconstruction, we decided to use the common method used in a stan-  
580 dard TPC (similar to?, cite some source(s)!). This will allow us to explore  
581 the significance of the atypical behavior in our OFTPC. Additionally, we assume  
582 the readout is continuous to further simplify the problem. In this approximation,  
583 we reconstruct the initial position of each ionization electron.

584 The reconstruction is then defined by the following relations between the co-  
585 ordinates of the detector space and the readout space (see Section 1.3.2): (some  
586 figure, maybe already relating to some track so that it's not too dull)

$$x = x', \quad (3.1)$$

$$y = y', \quad (3.2)$$

$$z = 8 \text{ cm} - d_r = 8 \text{ cm} - v_d t, \quad (3.3)$$

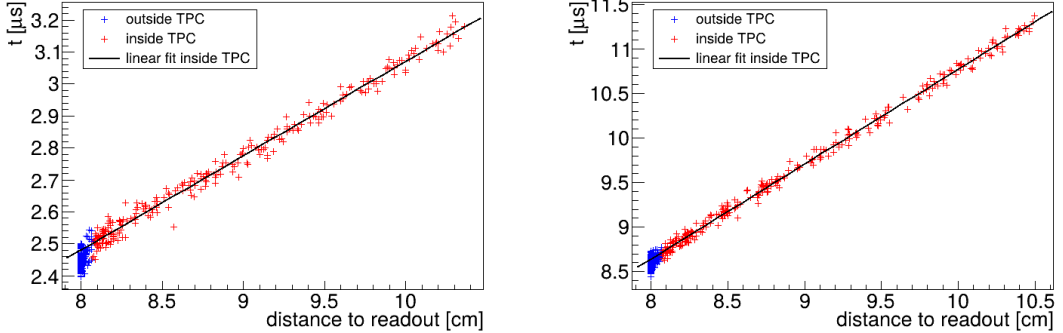


Figure 3.1: Linear fit of the drift time  $t$  dependence on the distance to the readout  $d_r = 8 \text{ cm} - z$  for the ionization electrons in 90:10 (left) and 70:30 (right) Ar:CO<sub>2</sub> gas composition. Only electrons inside the TPC (red) are fitted. The parameters are  $v_d = 3.39 \text{ cm}/\mu\text{s}$ ,  $d_0 = -0.41 \text{ cm}$  for 90:10, and  $v_d = 0.939 \text{ cm}/\mu\text{s}$ ,  $d_0 = -0.11 \text{ cm}$  for 70:30 Ar:CO<sub>2</sub>.

587 where  $d_r$  is the distance to the readout, and  $v_d$  is the drift velocity of electrons  
 588 in the given gas mixture. At a phenomenological level, this velocity can be con-  
 589 sidered as a function of the electric field  $\mathbf{E}$  and the magnetic field  $\mathbf{B}$  as shown in  
 590 Equation 1.1. **The Garfield++ toolkit uses this fact to accelerate their drift sim-  
 591 ulation with non-microscopic approaches (could mention in the simulation chapter).**  
 592 Since we assume a uniform electric field in the detector and in this approximation  
 593 we want to neglect the effect of our unusual magnetic field, we consider the drift  
 594 velocity constant. We can estimate the drift velocity by fitting the dependence  
 595  $d_r(t)$  of ionization electrons from a simulated track with a linear function:

$$d_r(t) = v_d t + d_0. \quad (3.4)$$

596 The fit was applied on two tracks with different gas composition, the result is in  
 597 Figure 3.1. **Compare with real drift velocities – a good indication of the tilt of**  
 598 **drift lines.** The obtained parameters are then used for the reconstruction shown  
 599 in Figure 3.2. From the residuals shown in Figure 3.3, we can see that this recon-  
 600 struction algorithm leads to significant deviations from the simulated track (up  
 601 to 1.1 cm for 90:10, and up to 0.3 cm for 70:30 Ar:CO<sub>2</sub>), especially in the faster  
 602 gas mixture 90:10 (as expected – for a higher mean time between collisions in  
 603 Equation 1.1, the effect of the magnetic field is bigger). These deviations are  
 604 mainly caused by the shift in the  $x$ -coordinate due to the tilt of the drift lines  
 605 in magnetic field. In order to account for this, we need to develop a better algo-  
 606 rithm. **There is also a small irregularity in the  $z$ -coordinate but it is comparable**  
 607 **with the diffusion. We can/will also later show that this has a significant effect**  
 608 **on the reconstructed energy.**

## 609 3.2 Ionization Electron Map

610 Inside an OFTPC ( $\exists$  more than one, also considering it a general concept rather  
 611 than the specific OFTPC used at this experiment), the drift of the secondary  
 612 (ionization) electrons is significantly affected by its magnetic field (**pictures of**  
 613 **the distortion later, the effect is bigger for the 90/10 composition**). We need to

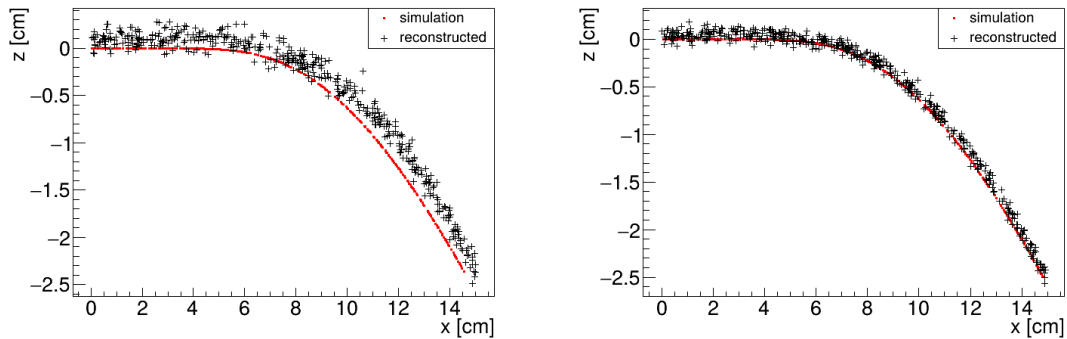


Figure 3.2: Reconstruction (black) of the starting position of ionization electrons (red) using parameters obtained from the fit (Figure 3.1). Two gas compositions 90:10 (left) and 70:30 Ar:CO<sub>2</sub> (right) are compared.

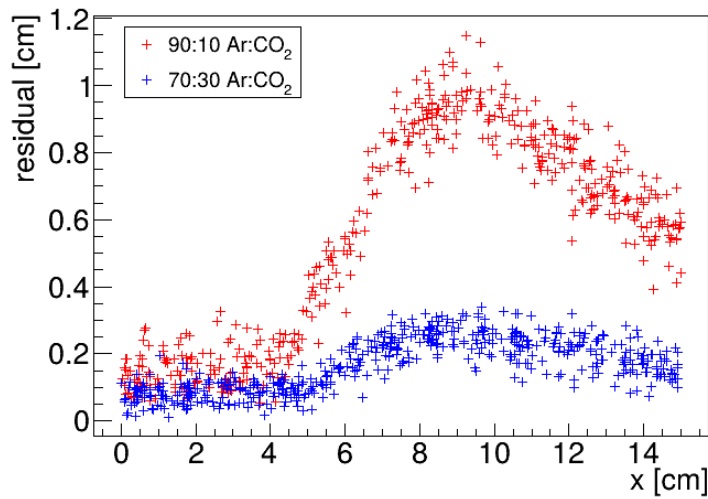


Figure 3.3: Comparison of residuals (i.e., the distance from the reconstructed point to the simulated ionization electron starting point) dependence on  $x$  for two gas mixtures 90:10 (red) and 70:30 Ar:CO<sub>2</sub> (blue).

614 take this into account for accurate reconstruction (should be easy to run the re-  
 615 construction without the map and show how much it improves the results). In  
 616 the first approximation, we assume a continuous readout (i.e., we neglect the an-  
 617 ode segmentation into pads). We can then reconstruct the original position of  
 618 each ionization electron using its readout coordinates. For this purpose, we use  
 619 the ionization electron map.

620 The ionization electron map represents a mapping from the detector space  
 621 to the readout space (see Section 1.3.2). It tells us what readout coordinates  
 622 ( $x', y', t$ ) we can expect on average for an ionization electron created at the de-  
 623 tector coordinates ( $x, y, z$ ). More precisely, it is a mapping to the distributions  
 624 on the readout space; we can simplify this as only the means  $\bar{\mathcal{M}}$  (inconsistent  
 625 notation in the text, write the bar everywhere or nowhere) and the covariance  
 626 matrices  $\mathcal{M}_{\text{cov}}$ , assuming Gaussian distribution (test this – some chisq or other  
 627 statistical test).

$$\bar{\mathcal{M}} : \mathcal{D} \longrightarrow \mathcal{R}, (x, y, z) \longmapsto (\bar{x}', \bar{y}', \bar{t}). \quad (3.5)$$

628 To get an approximation of this mapping, we simulate the drift of ionization  
 629 electrons generated on a regular grid inside the volume of our OFTPC<sup>1</sup>. In  
 630 order to get accurate results, we use the microscopic simulation of these electrons  
 631 described in Section 2.1 (Monte Carlo from *AvalancheMC* was also considered  
 632 but it doesn't (didn't?) include magnetic field, we can probably improve this  
 633 anyway using the fast track simulation with map proposed in the future section).  
 634 It is also useful to simulate multiple (100 in our case, this should really only be in  
 635 a table since there are two map simulations) electrons originating from the same  
 636 position so that we can account for the random fluctuations due to collisions.

637 When evaluating the map inside the grid, we use trilinear interpolation (see  
 638 Section 1.3.3). From now on, we will use the same symbol  $\mathcal{M}$  for this interpolated  
 639 simulation.

640 Finally, we need to invert the map to get the original detector coordinates  
 641 ( $x, y, z$ ) from the given readout coordinates ( $x', y', t$ ). In our case, it is reasonable  
 642 to assume that the mapping  $\bar{\mathcal{M}}$  (of means (notation inconsistency), we lose the  
 643 information about the distribution (a wild idea how to recover this is in the Future  
 644 section but it will only make sense if the GEM is already accounted for and is  
 645 very preliminary as there are many factors to consider)) is one-to-one (as seen in  
 646 the simulations). We implemented two methods for this purpose: the gradient  
 647 descent search (Section 3.2.1) and interpolation on the inverse grid (Section 3.2.2).

648 The simulation (?) of the map is a computationally heavy task. For this rea-  
 649 son, we use the MetaCentrum grid [3] to parallelize needed calculations. At first,  
 650 this was done by evenly distributing the simulated electrons across the individual  
 651 jobs in a simulation with only one electron per vertex in the regular grid with  
 652 a spacing of one centimeter. Later, a more efficient approach was implemented,  
 653 accounting for the varying lengths of the drift of individual electrons. If we in-  
 654 dex the electrons in the order of increasing coordinates  $y, x, z$  (picture will make  
 655 things clearer), we can express the number  $n_l$  of full XY layers (i.e., electrons

---

<sup>1</sup>The detector walls are not considered and we simulate the drift even outside of the OFTPC which allows us to interpolate even close to the walls

656 with the same  $z$  coordinate) of electrons with index less than or equal to  $i$

$$n_l(i) = \left\lfloor \frac{i}{n_{xy}} \right\rfloor, \quad (3.6)$$

657 where  $n_{xy}$  is the number of electrons in each XY layer calculated simply by counting  
658 the electrons that satisfy boundary conditions for  $x$  and  $y$ . These conditions  
659 should be mentioned above; sector condition + maximal  $x$  value. The number of  
660 electrons remaining in the top layer is then

$$n_r(i) = i \bmod n_{xy}. \quad (3.7)$$

661 Finally, we can calculate the sum of the drift gaps of electrons up to index  $i$

$$d_{\text{sum}} = (z_{\max} - z_{\min})n_{xy}n_l - \frac{n_l(n_l - 1)}{2}n_{xy}l + n_r(z_{\max} - z_{\min} - n_l l). \quad (3.8)$$

662 We then use a binary search algorithm to find the maximum index  $i$  such that  
663 the value of this sum is less than the fraction  $\frac{\text{job id}}{\max \text{job id}}$  of the total sum. This way  
664 we obtain the minimal and the maximal index of electrons simulated in the given  
665 job. The spacing  $l$  should be probably defined above + picture of the simulating  
666 grid (1 layer). zmin zmax also

667 After the simulation of the map, we calculate the mean readout coordinates  
668 assuming Gaussian distribution (i.e., we use averages). We also calculate standard  
669 deviations in a later commit, should be upgraded to the covariance matrix. We  
670 never actually plotted the distributions we get when simulating the same electron  
671 multiple times, so we do not know if our assumptions are accurate (could also  
672 run some statistical test to see how well the Gaussian distribution fits).

673 The obtained map is then stored in a custom class template *Field*, could  
674 expand on that. Maybe earlier, since the same template is used for the magnetic  
675 field.

676 Could insert a table here describing all 4 simulations of the map (gas composition,  
677 spacing, etc.). Simulation inside of one sector (at first double angle). Extra  
678 space on the sensor. Edge cases not taken into account (TPC wall). Using qsub  
679 (not sure if important). Add plots of distortion of the coordinates. Could also do  
680 these plots in a different way (e.g., drawing all the endpoints of each ionization  
681 electron or some error ellipse plot).

682

683 Images to add (comparison of both simulations):

- 684 • Already have a simple 2D map visualization from the RD51 presentation,  
685 can use it or make something better
- 686 • 3D visualization of the map, simulation example
- 687 •  $z$  vs.  $t$  plot
- 688 • XY plane distortion for different  $z$  values; with arrows and error bars, for  
689 all  $z$ -layers with different colors
- 690 • XZ plane ( $y = 0$ ) distortion in  $x$  (maybe not necessary?)
- 691 • XT plot ( $y = 0$ ) showing (small) distortion in drift times

692

693 More images:

- 694 • Residuals of the continuous readout reconstruction.

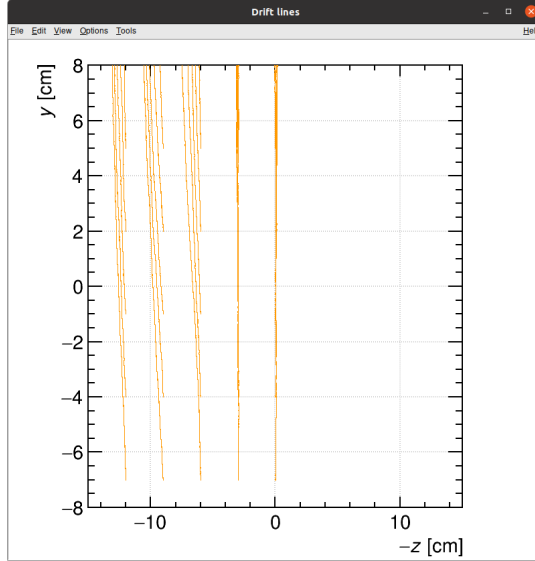


Figure 3.4: Example of map generation. Swap for better image, correct coordinates.

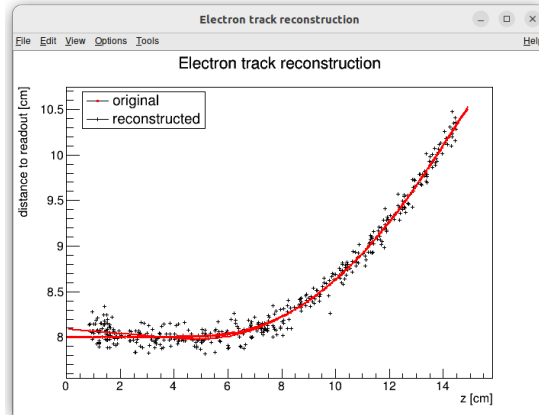


Figure 3.5: Example reconstruction with the map. Swap for better image, correct coordinates.

### 695 3.2.1 Gradient Descent Algorithm

696 The first implemented method of reconstruction uses a gradient descent algorithm  
697 to calculate an inversion of the map  $\bar{\mathcal{M}}$  in a given point. Gradient descent is  
698 an iterative minimization algorithm for multivariate functions. Let  $R \in \mathcal{R}$  be  
699 a point in the readout space; we want to find a point  $D = (x, y, z) \in \mathcal{D}$  in  
700 the detector space such that

$$\bar{\mathcal{M}}(D) = R = (x'_R, y'_R, t_R). \quad (3.9)$$

701 We define a function  $f_R$  in the readout space as a distance in this space:

$$f_R(x', y', t) = \sqrt{(x' - x'_R)^2 + (y' - y'_R)^2 + v_d^2(t - t_R)^2}, \quad (3.10)$$

702 where  $v_d$  is an approximation of the drift velocity in the TPC, obtained from  
 703 the reconstruction in Section 3.1 (there will be an image with the linear fit here).  
 704 We make an initial guess (actually in the original code we just take  $z = 0$ ):

$$D_0 = (x'_R, y'_R, v_d t). \quad (3.11)$$

705 Assuming we have the  $n$ -th estimate  $D_n$ , we calculate the  $i$ -th component of  
 706 the gradient of  $f_R \circ \bar{\mathcal{M}}$  numerically using central differences: (signs look correct)

$$[\nabla(f_R \circ \bar{\mathcal{M}})]^i(D_n) \approx \frac{f_R(\bar{\mathcal{M}}(D_n + s \cdot e^i)) - f_R(\bar{\mathcal{M}}(D_n - s \cdot e^i))}{2s}, \quad (3.12)$$

707 where  $e^i \in \mathcal{D}$  is the  $i$ -th coordinate vector and  $s$  is the step size. The step size  
 708 should be sufficiently small; initially, we set it as a fraction  $s = \frac{l}{10}$  of the map's  
 709 grid spacing  $l$ . During the minimization, we check that  $f_R(\bar{\mathcal{M}}(D_n)) < 10s$  at all  
 710 times (s can (?) change – check). When using trilinear interpolation, it would be  
 711 more efficient to calculate the gradient explicitly ( $\pm$  same result). This could be  
 712 implemented inside the *Field* template class. The next iteration can be calculated  
 713 as follows:

$$D_{n+1} = D_n - \gamma \nabla(f_R \circ \bar{\mathcal{M}})(D_n), \quad (3.13)$$

714 where  $\gamma \in \mathbb{R}^+$  is the damping coefficient. It should be set to a small enough  
 715 value to ensure convergence, but large enough for sufficient converging speed.  
 716 The minimization stops either when the error  $f_R(\bar{\mathcal{M}}(D_n))$  drops below a specified  
 717 value or when the number of iterations exceeds a certain limit (in this case,  
 718 a message is printed into the console). The parameters of this method can be  
 719 further optimized (e.g., a better choice of  $\gamma$ , gradient computation); instead, we  
 720 later decided to use the interpolation on the inverse grid described in the next  
 721 section.

722 Measure reconstruction duration and compare it with the inverse grid inter-  
 723 polation? Also compare the result? Typical evolution of  $D_n$  during search. Not  
 724 sure if this has to be cited.

### 725 3.2.2 Interpolation on the Inverse Grid

726 Interpolation should be generally faster than the gradient descent since we don't  
 727 need to iterate. We also don't need to optimize it to improve performance, if  
 728 it's too slow we can even calculate the coefficients for the entire map before  
 729 reconstruction (again, do some profiling).

730 The best current algorithm uses the interpolation on the inverse grid. Rather  
 731 than inverting the trilinearly interpolated map using a numerical minimization  
 732 method as in the previous section, we take advantage of the fact that the map  
 733  $\bar{\mathcal{M}}$  is one-to-one (isomorphism is supposed to preserve structure, not sure how  
 734 to interpret that here, not the best description, we already (kind of) assume it  
 735 is a bijection by saying we will invert it). Since we have simulated values of this  
 736 map on a regular grid in the detector space  $\mathcal{D}$ , we also know the inverse map  $\bar{\mathcal{M}}^{-1}$   
 737 on the irregular inverse grid in the readout space  $\mathcal{R}$ . To get an approximation  
 738 of the inverse map in the entire readout space, we can use interpolation (general  
 739 concept, the specific choice is described below).

740 Since the inverse grid is irregular, trilinear interpolation cannot be applied.  
 741 Given that the simulated map is dense enough to provide a good approximation

742 considering the size of our pads, we can adopt a similar approach.<sup>2</sup> As shown in  
 743 Equation 1.20 in Section 1.3.3, trilinear interpolation (shouldn't need an article  
 744 when talking about a general concept) can be expressed as a polynomial:

$$\hat{f}(x, y, z) = axyz + bxy + cxz + dyz + ex + fy + gz + h, \quad (3.14)$$

745 where  $a, b, c, d, e, f, g, h$  are coefficients uniquely determined by the values of  
 746 the function at the vertices of the interpolation cell (can be calculated in the  
 747 way shown in the mentioned equation, not sure what more to add). We can gen-  
 748 eralize this for a function defined on an irregular grid. Given the function values  
 749 at any eight points, we can write a system of eight linear equations

$$\begin{pmatrix} x_1y_1z_1 & x_1y_1 & x_1z_1 & y_1z_1 & x_1 & y_1 & z_1 & 1 \\ \vdots & \vdots \\ x_8y_8z_8 & x_8y_8 & x_8z_8 & y_8z_8 & x_8 & y_8 & z_8 & 1 \end{pmatrix} \begin{pmatrix} a \\ \vdots \\ h \end{pmatrix} = \begin{pmatrix} f(x_1, y_1, z_1) \\ \vdots \\ f(x_8, y_8, z_8) \end{pmatrix}, \quad (3.15)$$

750 which has a unique solution for the coefficients for most values of  $(x_n, y_n, z_n)$  and  
 751  $f(x_n, y_n, z_n)$ , where  $n \in \{1, \dots, 8\}$ .

752 This approach introduces a small complication: finding the correct pseudo-  
 753 cell (i.e., the image of eight vertices forming a cubic cell in the regular grid) in  
 754 the inverse grid. The eight irregularly spaced vertices of this pseudocell do not  
 755 define a unique volume, so there are multiple possible ways to partition  $\mathcal{R}$  into  
 756 pseudocells, with no obvious choice among them.

757 We are currently ignoring this problem and performing binary search along  
 758  $x, y, z$  (in this order). It shouldn't matter too much because the 70/30 map  
 759 doesn't cause such a big distortion and was even accidentally extrapolated for all  
 760  $z$  different from the central plane.

---

<sup>2</sup>A more complicated and computationally heavy alternative would be natural neighbor interpolation or Kriging.

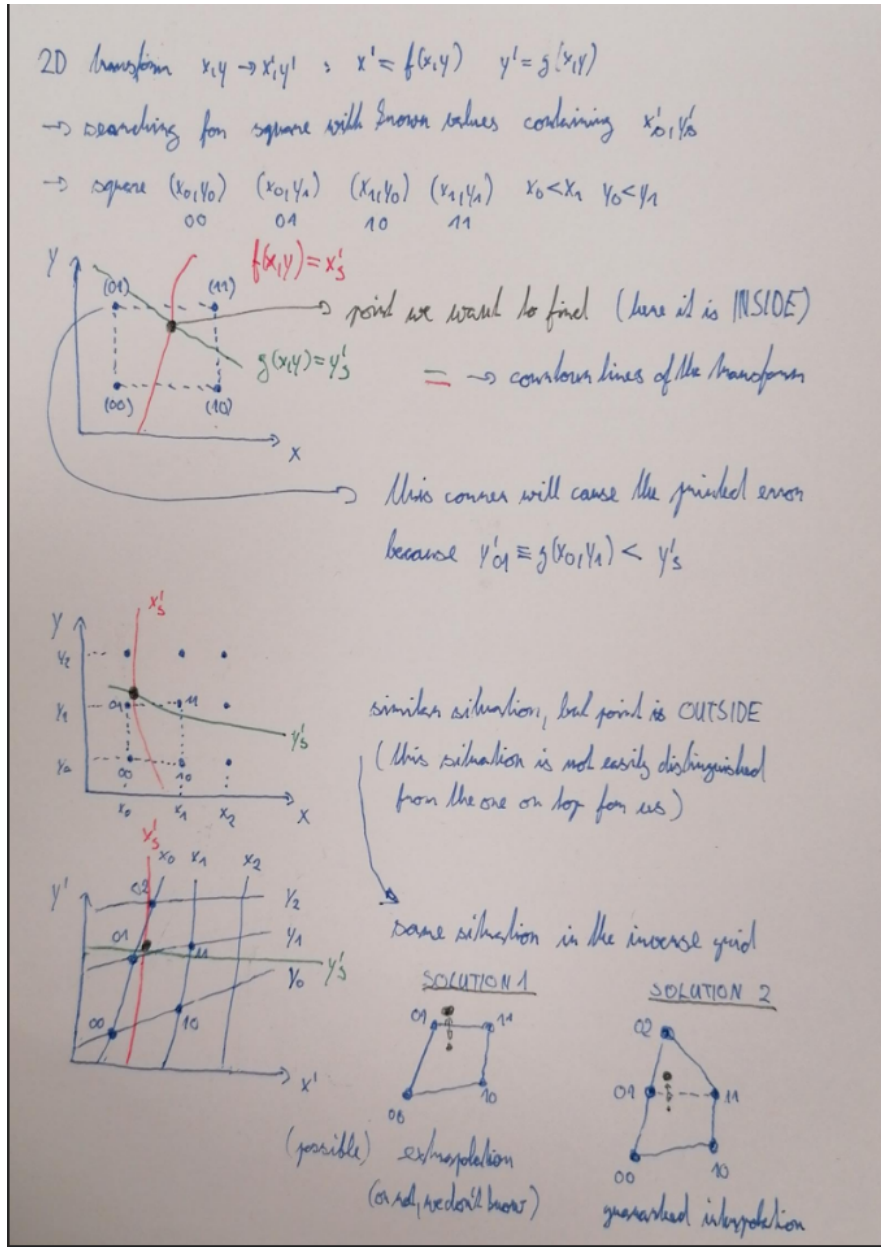


Figure 3.6: Selection of the points for interpolation. Create better images; use the explanation interpolation vs. extrapolation strange property. Solution 2 probably does not make much sense.

### 761 3.3 Discrete Reconstruction

762 Reconstruction with pads and time bins. Maybe testing different pads.

763 It is also possible to make this a subsection of the map, making the previous  
764 subsections parts of a new subsection 'Map Inversion'.

765 In order to get a more realistic representation of a track measured in the OFTPC,  
766 we need to take the discretization of the position and time data into account.  
767 The readout of the OFTPC will consist of 128 pads, their layout is shown in  
768 Figure 1.6. Time is read out in discrete bins of size  $t_{\text{bin}} = 100$  ns.

769 As the first approximation, we can neglect the multiplication in the triple-GEM.

770 and assume an ideal charge readout. The time measurement starts at the begin-  
 771 ning of the electron/positron simulation (depending on the specific simulation it  
 772 can correspond to the production in the target or when entering the OFTPC,  
 773 here the specific time doesn't matter too much since the primary particle trav-  
 774 els basically at light speed (30 ps/cm) which is circa immediate given the time  
 775 binning). Randomize this time a bit and see what it does to the reconstruction.  
 776 The readout coordinates  $(x', y', t) \in \mathcal{R}$  of each ionization electron can be mapped  
 777 to the pad coordinates  $(n_{\text{pad}}, n_t) \in \mathcal{P}$ :

$$n_{\text{pad}} = n: (x', y') \in \left[ x_{1,n} - \frac{g}{2}, x_{2,n} + \frac{g}{2} \right] \times \left[ y_{1,n} - \frac{g}{2}, y_{2,n} + \frac{g}{2} \right], \quad (3.16)$$

$$n_t = \left\lceil \frac{t}{t_{\text{bin}}} \right\rceil, \quad (3.17)$$

778 where  $x, y_{1,n}$  and  $x, y_{2,n}$  are the opposing pad corner coordinates, and  $g$  is the  
 779 gap between the pads (described in detail in Section 1.3.2). This way, the clos-  
 780 est pad is assigned to each readout position within the OFTPC volume<sup>3</sup>. Makes  
 781 sense since the pads attract the electrons, the inhomogeneity of electric field is  
 782 neglected. The number of electrons collected by each pad (i.e., collected charge)  
 783 in each time bin is then counted and serves as a weight for the energy recon-  
 784 struction. The reconstructed track consists of points for each  $(n, n_t) \in \mathcal{P}$ , we get  
 785 these by reconstructing the position of a hypothetical electron with the readout  
 786 coordinates of the pad/time bin center:<sup>4</sup>

$$\mathcal{D} \ni (x, y, z) = \overline{\mathcal{M}} \left( x_{c,n}, y_{c,n}, \left( n_t - \frac{1}{2} \right) t_{\text{bin}} \right). \quad (3.18)$$

---

<sup>3</sup>Some positions near the wall are not handled and some pads extend beyond the OFTPC volume. This is where an electric field simulation would come in handy.

<sup>4</sup>Mapping the center of the pad (along with the midpoint of the time bin) isn't necessarily the best approach since it might not correspond to the average parameters of an electron with these readout parameters.

## 4. Energy Reconstruction

The second stage is the reconstruction of the particle's energy using a fit of its reconstructed track (see Section 3). We have tested three ways of reconstructing the energy. Fitting is done using the MINUIT algorithm implemented in ROOT [2]. Cite some CERN article directly on MINUIT, can add a section. Or is it done using MIGRAD? The circle and RK4 probably was.

The **Cubic Spline Fit** was a tested and later rejected method of energy reconstruction. It uses smoothly connected piecewise cubic polynomials between uniformly spaced nodes. The reconstructed energy is calculated using the fit parameters by computing the radius of curvature in different points of the fitted curve using the known magnitude of the magnetic field perpendicular to the trajectory. We rejected this method because the tuning of the fit turned out to be unpractical compared to the other used methods. Reconstructs energy at every position (even though the actual energy doesn't change much) and it might be slower but no profiling has been done yet. Of course, it wasn't tested on the newer track reconstruction methods at all.

The **Circle and Lines Fit** was chosen as an alternative since this corresponds to the shape of a trajectory of a charged particle crossing a finite volume with a homogeneous magnetic field. The energy of the particle can be estimated using the fitted radius and the magnitude of the perpendicular magnetic field in the middle of the TPC.

The **Runge-Kutta Fit** uses the 4th order Runge-Kutta numerical integration described in Section 2.2. Initial parameters of the track (including the particle's energy) are optimized so that the integrated trajectory fits to the reconstructed one. This fit can also be performed as a single parameter (i.e., energy) fit if we get the initial position and orientation of the particle on the entrance to the TPC from previous detectors (TPX3 and MWPC, see Section 0.2).

### 4.1 Cubic Spline Fit

The first method for the estimation of the kinetic energy of the particle uses a cubic spline fit. We use an electron track simulated using the microscopic

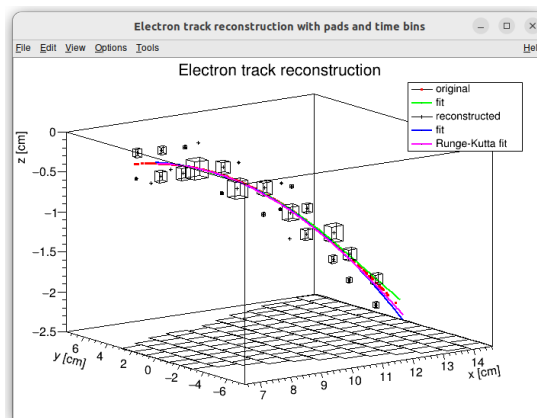


Figure 4.1: Example of a fitted reconstructed track. Swap for better image.

simulation, described in detail in Section 2.1.1. The track was reconstructed using the map described in Section 3.2.

In order to calculate the spline, we use the class *TSplines3* from ROOT. This allows us to evaluate the spline using the coordinates  $(x_n, z_n)$  of each node and the derivatives  $d_1, d_2$  in the first and the last node. We can fit these parameters of a fixed amount of nodes to the simulated trajectory. We use the IMPROVE algorithm provided by the *TMinuit* class in ROOT (there are some guidelines for fonts in MFF UK template (Czech version) that I will eventually apply (see notes in the conclusion)). This algorithm attempts to find a better local minimum after converging (could reformulate a bit, taken word for word from some manual).

After the fit converges, we calculate an energy estimate using the radius of curvature, which we can extract from the fitted spline equation at every point of the trajectory. The part of the spline corresponding to a given node is defined as

$$z(x) = z_n + b\Delta x + c(\Delta x)^2 + d(\Delta x)^3, \quad (4.1)$$

where  $\Delta x = x - x_n$  and  $b, c, d$  are coefficients. Using this equation, we derive the radius of curvature<sup>1</sup> as:

$$r(x) = \frac{(1 + z'^2(x))^{\frac{3}{2}}}{z''(x)} = \frac{(1 + (b + 2c\Delta x + 3d(\Delta x)^2)^2)^{\frac{3}{2}}}{2c + 6d\Delta x}. \quad (4.2)$$

Based on the geometry of our detector, we assume that the magnetic field satisfies  $\mathbf{B}(x, 0, z) = (0, B(x, z), 0)$  for a track in the XZ plane. Since the electron is relativistic, the effect of the electric field on its trajectory is negligible. The Lorentz force  $F_L$  is then always perpendicular to the momentum of the electron and acts as a centripetal force  $F_c$  (not quite sure how to handle this then?):

$$\begin{aligned} \mathbf{F}_L &= \mathbf{F}_c, \\ \|e\mathbf{v} \times \mathbf{B}\| &= \frac{\gamma m_e v^2}{r}, \\ ec\beta B &= \frac{E_{0e}\beta^2}{r\sqrt{1 - \beta^2}}, \end{aligned} \quad (4.3)$$

$$\sqrt{1 - \beta^2} = \frac{E_{0e}\beta}{ecBr}, \quad (4.4)$$

$$\beta^2(x) = \left[ 1 + \left( \frac{E_{0e}}{ecB(x, z(x))r(x)} \right)^2 \right]^{-1}, \quad (4.4)$$

where  $e$  is the elementary charge,  $c$  is the speed of light in vacuum,  $m_e$  is the rest mass of electron,  $E_{0e} = m_e c^2$  is its rest energy,  $\gamma$  is the Lorentz factor,  $\mathbf{v}$  is the velocity of the electron, and  $\beta = \frac{v}{c}$ . The kinetic energy for a given point on the trajectory is then given as

$$E_{\text{kin}}(x) = \left( \frac{1}{\sqrt{1 - \beta^2(x)}} - 1 \right) E_{0e}. \quad (4.5)$$

---

<sup>1</sup>For the general formula see [https://en.wikipedia.org/wiki/Curvature#Graph\\_of\\_a\\_function](https://en.wikipedia.org/wiki/Curvature#Graph_of_a_function).

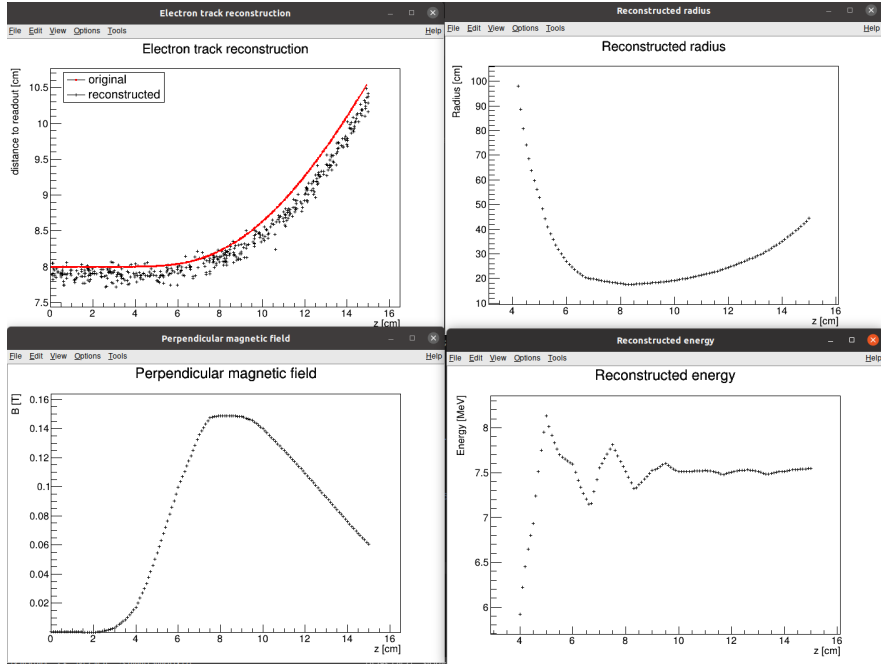


Figure 4.2: First attempt at a track reconstruction using only the drift velocity. Spline energy reconstruction attempt. Swap for better image(s) – subfigure environment, correct coordinates.

841 We can then average these estimates at multiple points (possibly using some  
 842 weights to account for the change in accuracy, this wasn't optimized and we just  
 843 ended with the graph) to get a single value. This method was later rejected in  
 844 favor of the circle and lines fit (the name was already established at the beginning  
 845 of the chapter) described in the next section. Add some figures.

## 846 4.2 Circle and Lines Fit

847 Another way to estimate the particle's kinetic energy is to fit its (??) trajectory  
 848 with a circular arc with lines attached smoothly. This shape of trajectory cor-  
 849 responds to a movement of a charged particle through a homogeneous magnetic  
 850 field perpendicular to the particle's momentum and limited to a certain volume.  
 851 In general, the shape of such a trajectory with a non-perpendicularly oriented  
 852 momentum is a spiral. In our case, the magnetic field is approximately toroidal  
 853 and the particle motion is nearly perpendicular to it (verify, could add some  
 854 magnetic field plots in different vertical planes; shouldn't have a big effect on the  
 855 reconstructed radius anyway). At first, we tested a 2D version of this fit, then  
 856 we adapted it to 3D.

857 The field in our detector is not homogeneous, it is therefore not entirely clear  
 858 what value of magnetic field should be used along with the fitted radius (using  
 859 equations 4.4 and 4.5) to get the best estimate for the kinetic energy. Since we  
 860 only use this method as the first iteration of the particle's energy that we later  
 861 refine, an optimal solution of this problem is not required. Instead, we tested two  
 862 options: taking the value of the field in the middle of the fitted circular arc (or  
 863 is it in the middle  $x$  of the OFTPC?) and taking the average field along it. We

haven't really tried to plot this for multiple tracks, but these estimates are saved somewhere and could be plotted.

### 4.2.1 Two-dimensional fit

In the 2D case, the fitted function used for the electron track<sup>2</sup> described in Section 2.1.1 (one specific track at the time, technically this function doesn't work for a curvature that gets outside of the semicircle) is defined as follows:

$$z(x) = \begin{cases} a_1x + b_1 & x < x_1 \\ z_0 + \sqrt{r^2 - (x - x_0)^2} & x_1 \leq x \leq x_2 \\ a_2x + b_2 & x > x_2 \end{cases}, \quad (4.6)$$

where  $a_{1,2}$  and  $b_{1,2}$  are the parameters of the lines,  $(x_0, z_0)$  is the center of the circle,  $r$  is its radius, and  $(x_{1,2}, z_{1,2})$  are the coordinates of the function's nodes. That means we have 9 parameters ( $z_{1,2}$  are not used in the function) along with 2 continuity conditions and 2 smoothness conditions (9 parameters of the described function, 5 of them independent after taking the conditions into account). For the fit, we use the coordinates of the nodes and the radius of the circle, which gives us 5 independent parameters (only the radius has to be larger than half of the distance between nodes). The continuity conditions (combined with the relations for  $z_{1,2}$ ) are

$$z_{1,2} = a_{1,2}x_{1,2} + b_{1,2} = z_0 - \sqrt{r^2 - (x_{1,2} - x_0)^2}, \quad (4.7)$$

the smoothness conditions are

$$a_{1,2} = \frac{x_0 - x_{1,2}}{\sqrt{r^2 - (x_{1,2} - x_0)^2}}. \quad (4.8)$$

Together with the Equation 4.7 we get the values of  $b_{1,2}$

$$b_{1,2} = z_{1,2} - a_{1,2}x_{1,2}. \quad (4.9)$$

For the coordinates of the center of the circle, we can use the fact that the center has to lie on the axis of its chord. In other words, there is a value of a parameter  $t$  such that, using the parametric equation of the axis

$$\begin{pmatrix} x_0 \\ z_0 \end{pmatrix} = \begin{pmatrix} \frac{x_1+x_2}{2} \\ \frac{z_1+z_2}{2} \end{pmatrix} + t \begin{pmatrix} \frac{z_2-z_1}{2} \\ \frac{x_1-x_2}{2} \end{pmatrix}. \quad (4.10)$$

At the same time, the center has to be in a distance of  $r$  from the nodes:

$$\begin{aligned} (x_1 - x_0)^2 + (z_1 - z_0)^2 &= r^2, \\ \left( \frac{x_1 - x_2}{2} + \frac{z_1 - z_2}{2}t \right)^2 + \left( \frac{z_1 - z_2}{2} + \frac{x_2 - x_1}{2}t \right)^2 &= r^2, \\ \left( \left( \frac{x_2 - x_1}{2} \right)^2 + \left( \frac{z_2 - z_1}{2} \right)^2 \right)t^2 + \left( \frac{x_2 - x_1}{2} \right)^2 + \left( \frac{z_2 - z_1}{2} \right)^2 - r^2 &= 0. \end{aligned} \quad (4.11)$$

---

<sup>2</sup>Electron tracks bend towards negative  $z$ , we need to use the upper part of the circle

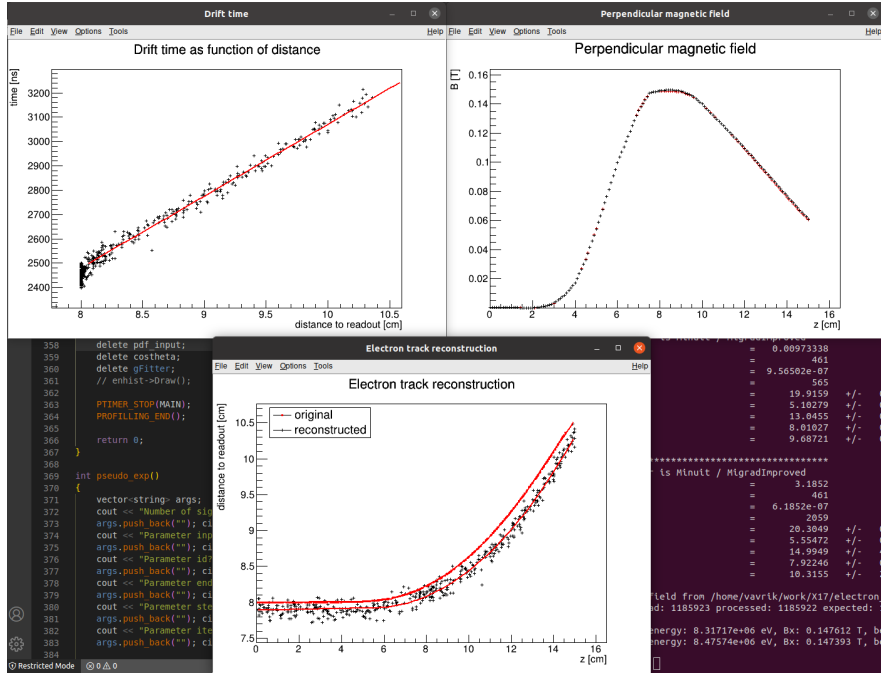


Figure 4.3: First attempt at a track reconstruction using only the drift velocity. Circle and Lines Fit in 2D. Swap for better image, correct coordinates. Bias should be described in the previous chapter, not here.

885 Since our electron track bends towards negative  $z$  and  $x_2 > x_1$ , we only care  
886 about the solution with  $t > 0$

$$t = \sqrt{\frac{r^2}{\left(\frac{x_2-x_1}{2}\right)^2 + \left(\frac{z_2-z_1}{2}\right)^2} - 1}, \quad (4.12)$$

$$x_0 = \frac{x_1 + x_2}{2} + \frac{z_2 - z_1}{2} \sqrt{\frac{r^2}{\left(\frac{x_2-x_1}{2}\right)^2 + \left(\frac{z_2-z_1}{2}\right)^2} - 1}, \quad (4.13)$$

$$z_0 = \frac{z_1 + z_2}{2} - \frac{x_2 - x_1}{2} \sqrt{\frac{r^2}{\left(\frac{x_2-x_1}{2}\right)^2 + \left(\frac{z_2-z_1}{2}\right)^2} - 1}.$$

887 The function defined in Equation 4.6 along with equations 4.8, 4.9, and 4.13  
888 derived using the continuity and smoothness conditions (combined with the re-  
889 lations for  $z_{1,2}$ ) fully define our fitted function with parameters  $r, x_{1,2}, z_{1,2}$ . Some  
890 pictures of the fit on the tested track. Results of the fit. Again, the actual fit  
891 uses 8-z. Use GeoGebra schematics to generate a picture of 2D geometry.

### 892 4.2.2 Three-dimensional fit

893 Explain the geometry and least square method used for the 3D fit. Tested on  
894 a Runge-Kutta sample, and with microscopic tracks + map simulation.

895 In three dimensions, the shape of a trajectory of a charged particle in a uniform  
896 magnetic field is a cylindrical helix. Nevertheless, since we assume that the  
897 field is approximately perpendicular to the particle's momentum at all times, we

will further approximate the trajectory with a circular arc (with lines attached smoothly).

We assume that the initial position  $\mathbf{X}_0 = (x_0, y_0, z_0)$  and direction  $\theta, \varphi$  (spherical angles as in Section 1.3.2) are known, since this information will be provided by TPX3 and MWPC layers. We could further refine it at the end of the current algorithm with some kind of global fit (all detector layers). The fit then has four free parameters (figure):

- the length of the first line  $l$  (as measured from the initial position),
- the radius of the circular arc  $r$ ,
- the central angle of the arc  $\phi_{\max} \in [0, 2\pi]$ ,
- the direction of the curvature given by the angle  $\alpha \in [0, 2\pi]$  (right-handed with respect to the particle direction,  $\alpha = 0$  if the particle curves towards negative  $z$  in a plane given by  $\hat{\mathbf{z}}$  and the direction vector).

Using these parameters, we can derive a parametrization of the whole curve. Let  $\mathbf{v}$  be the initial unit direction vector, i.e., using the spherical angles

$$\mathbf{v} = (\cos \varphi \cos \theta, \sin \varphi \cos \theta, \sin \theta)^T, \quad (4.14)$$

then we can parameterize the first line as follows:

$$\mathbf{X}_{L1}(t) = \mathbf{X}_0 + t\mathbf{v} \quad t \in [0, l]. \quad (4.15)$$

This gives us the starting point of the arc

$$\mathbf{X}_1 = \mathbf{X}_{L1}(l) = \mathbf{X}_0 + l\mathbf{v}. \quad (4.16)$$

The vector  $\mathbf{c}_1$  that lies in the plane of curvature and points from  $\mathbf{X}_1$  to the center of curvature can be calculated using a composition of rotations. First, we rotate  $\mathbf{v}$  to point in the  $\hat{\mathbf{x}}$  direction, the normal for  $\alpha = 0$  than points in the  $-\hat{\mathbf{z}}$  direction, we apply the  $\alpha$  rotation and reverse the rotations into the  $\hat{\mathbf{x}}$  direction: (parameters are explained in the bullet points above)

$$\begin{aligned} \mathbf{c}_1 &= R_z(\varphi)R_y(-\theta)R_x(\alpha)R_y\left(\frac{\pi}{2}\right)R_y(\theta)R_z(-\varphi)\mathbf{v}, \\ &= R_z(\varphi)R_y(-\theta)R_x(\alpha)(-\hat{\mathbf{z}}), \\ &= \begin{pmatrix} \cos \varphi & -\sin \varphi & 0 \\ \sin \varphi & \cos \varphi & 0 \\ 0 & 0 & 1 \end{pmatrix} \begin{pmatrix} \cos \theta & 0 & -\sin \theta \\ 0 & 1 & 0 \\ \sin \theta & 0 & \cos \theta \end{pmatrix} \begin{pmatrix} 1 & 0 & 0 \\ 0 & \cos \alpha & -\sin \alpha \\ 0 & \sin \alpha & \cos \alpha \end{pmatrix} \begin{pmatrix} 0 \\ 0 \\ -1 \end{pmatrix}, \quad (4.17) \\ &= \begin{pmatrix} -\sin \alpha \sin \varphi + \cos \alpha \cos \varphi \sin \theta \\ \sin \alpha \cos \varphi + \cos \alpha \sin \varphi \sin \theta \\ -\cos \alpha \cos \theta \end{pmatrix}. \end{aligned}$$

Signs should be correct because right-handed rotation around  $y$  rotates  $z$  into  $x$  and this one is the opposite. Seems like in this part of the code  $\theta$  is actually taken from the pole. Instead of the equator plane. Similarly by rotating  $\hat{\mathbf{y}}$ , we can get the normal vector  $\mathbf{n} = \mathbf{v} \times \mathbf{c}_1$  perpendicular to the plane of the trajectory:

$$\mathbf{n} = R_z(\varphi)R_y(-\theta)R_x(\alpha)\hat{\mathbf{y}} = \begin{pmatrix} -\cos \alpha \sin \varphi - \sin \alpha \cos \varphi \sin \theta \\ \cos \alpha \cos \varphi - \sin \alpha \sin \varphi \sin \theta \\ \sin \alpha \cos \theta \end{pmatrix}. \quad (4.18)$$

924 This allows us to express the coordinates of the center  $\mathbf{C}$  of the circular arc:

$$\mathbf{C} = \mathbf{X}_1 + r\mathbf{c}_1. \quad (4.19)$$

925 We can then get the parametrization and the endpoint of the circular arc using  
926 Rodrigues' rotation formula: (all parameters explained in the bullet points above)

$$\begin{aligned} \mathbf{c}_2 &= \mathbf{c}_1 \cos \phi_{\max} + (\mathbf{n} \times \mathbf{c}_1) \sin \phi_{\max} + \mathbf{n}(\mathbf{n} \cdot \mathbf{c}_1)(1 - \cos \phi_{\max}), \\ &= \mathbf{c}_1 \cos \phi_{\max} - \mathbf{v} \sin \phi_{\max}, \end{aligned} \quad (4.20)$$

$$\mathbf{X}_C(\phi) = \mathbf{C} - r(\mathbf{c}_1 \cos \phi - \mathbf{v} \sin \phi) \quad \phi \in [0, \phi_{\max}], \quad (4.21)$$

$$\mathbf{X}_2 = \mathbf{X}_C(\phi_{\max}) = \mathbf{C} - r\mathbf{c}_2, \quad (4.22)$$

927 and if we define the direction vector of the second line, we also get its parametriza-  
928 tion

$$\mathbf{w} = \mathbf{v} \cos \phi_{\max} + (\mathbf{n} \times \mathbf{v}) \sin \phi_{\max} = \mathbf{v} \cos \phi_{\max} + \mathbf{c}_1 \sin \phi_{\max}, \quad (4.23)$$

$$\mathbf{X}_{L2}(s) = \mathbf{X}_2 + s\mathbf{w} \quad s \in [0, \infty). \quad (4.24)$$

929 The fit is performed as a (weighted) least square minimization (MIGRAD  
930 ROOT), therefore we need to derive the distance of any point  $\mathbf{P}$  to the fitted  
931 curve. For the first line, we simply compute the parameter value of the closest  
932 point on the line:

$$\begin{aligned} t_P &= \mathbf{v} \cdot (\mathbf{P} - \mathbf{X}_1), \\ d_{P1} &= \|\mathbf{P} - \mathbf{X}_{L1}(t_P)\|. \end{aligned} \quad (4.25)$$

933 If the parameter value is outside of its bounds defined above, we take the bound-  
934 ary value instead. The distance to the second line is computed likewise. For  
935 the circular arc (specific circular arc in the fit), we find the closest point (on the  
936 arc) by projecting the center connecting line onto the arc plane:

$$\mathbf{X}_{PC} = \mathbf{X}_C + r \frac{(\mathbf{P} - \mathbf{X}_C) - (\mathbf{n} \cdot (\mathbf{P} - \mathbf{X}_C))\mathbf{n}}{\|(\mathbf{P} - \mathbf{X}_C) - (\mathbf{n} \cdot (\mathbf{P} - \mathbf{X}_C))\mathbf{n}\|}, \quad (4.26)$$

$$d_{PC} = \|\mathbf{P} - \mathbf{X}_{PC}\| \quad (4.27)$$

937 Potential problem in the implementation – might not be correctly handling  $\phi$   
938 out of bounds, the distance could be sometimes underestimated because of this.

939 The shortest distance out of  $d_{P1}, d_{PC}, d_{P2}$  is then taken as the distance to the curve. When  
940 calculating energy with the average field, only the arc is considered. Middle field  
941 in the current implementation taken in the middle  $x$  plane (intersection with  
942 the curve). TVirtualFitter+MIGRAD, maximal num of iterations, toleration.  
943 Different uncertainties in  $x, y, z$  not taken into account.

944 Fit details (parameter bounds, initial setting).

### 945 4.2.3 Testing on a Runge-Kutta sample

946 The three dimensional circle and lines fit was tested on a sample of Runge-Kutta  
947 tracks with randomized parameters described in Section 2.2.1. These tracks of  
948 primary electrons and positrons consist of points calculated with the RK4 algo-  
949 rithm for a given proper time step (step can be adjusted by dividing by the gamma  
950 factor → detector time). Fitting with circle only was also partially implemented  
951 (didn't work but could be fixed/tuned).

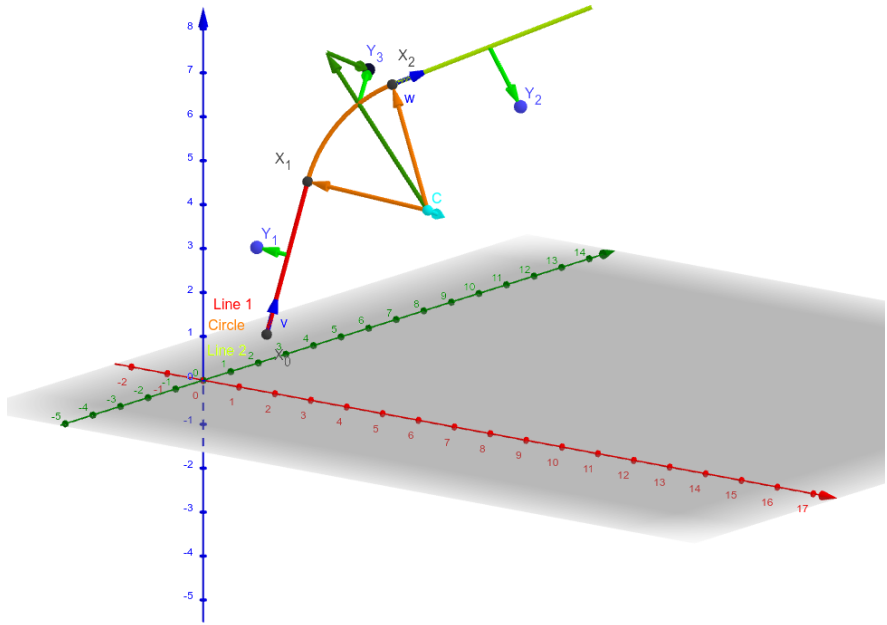


Figure 4.4: Circle and Lines Fit 3D geometry. Swap for better image.

### 952 4.3 Runge-Kutta Fit

953 The Runge-Kutta fit uses the Runge-Kutta 4th order (RK4) numerical integration  
 954 of the equation of motion (see Section 2.2) to find the best values of the track  
 955 parameters – the track origin, initial velocity direction and the kinetic energy. In  
 956 order to speed up the energy reconstruction, an initial guess of these parameters  
 957 can be obtained from the 3D circle fit described in the previous section. Fur-  
 958 thermore, assuming we know the track origin and orientation, we can perform  
 959 a single parameter fit of the kinetic energy (**do some profiling and show that it is**  
 960 **faster – below in the microscopic testing**).

961 The fit is performed as a least square minimization of the (weighted) distances  
 962 of the track points (true ionization vertices from the simulation or reconstructed  
 963 points). The simulated RK4 track consists of line segments with known endpoints,  
 964 therefore we can calculate the distance of a point from this segment analogically  
 965 to Equation 4.25 with  $\mathbf{v}$  given as a unit vector in the direction of the segment.

966 We need to find the segment with the lowest distance. We assume, that  
 967 the distance  $d_{\mathbf{P}}(\tau)$  of a point  $\mathbf{P}$  to the point on the track  $\mathbf{X}(\tau)$  has a single  
 968 minimum (local and global), no local maximum (except the interval endpoints)  
 969 and no saddle point

$$\exists! \tau_{\min} \in [0, \tau_N]: (\forall \tau \in [0, \tau_N]: d_{\mathbf{P}}(\tau) \geq d_{\mathbf{P}}(\tau_{\min})) \vee \frac{dd_{\mathbf{P}}}{d\tau}(\tau_{\min}) = 0, \quad (4.28)$$

970 where  $N$  is the number of RK4 steps. This is a reasonable assumption for a track  
 971 with an approximate shape of a circular arc with a radius  $r$ , since the distance  $d$   
 972 from a point  $\mathbf{C}$  on the corresponding circle of a point  $\mathbf{P}$  offset by  $a$  from the arc  
 973 plane and by  $b$  from the arc's center when projected on its plane is given by the

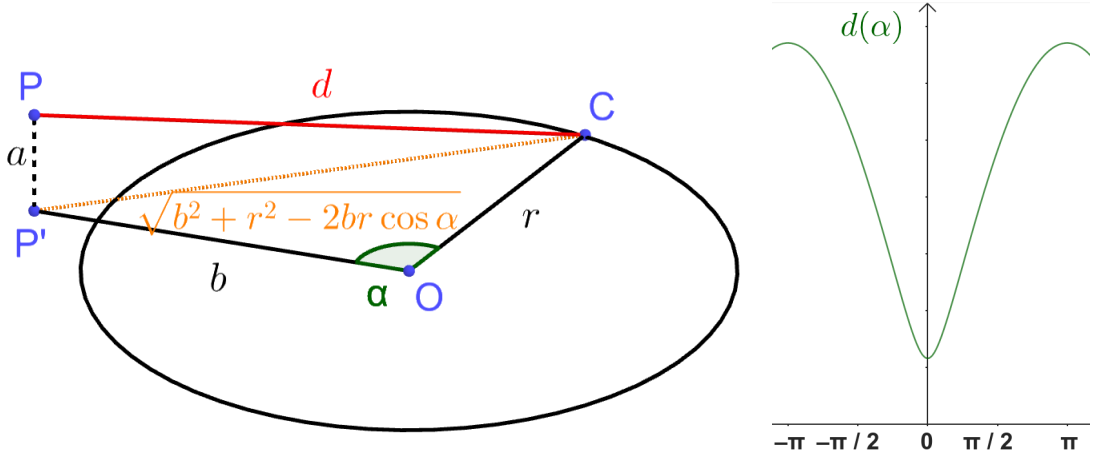


Figure 4.5: Demonstration of the convexity of the distance function  $d(\alpha)$  for a circular track (see Equation 4.29).

974 law of cosines:

$$d^2 = a^2 + b^2 + r^2 - 2br \cos \alpha, \quad (4.29)$$

975 where  $\alpha$  is the angle between points  $\mathbf{C}$  and  $\mathbf{P}$  as seen from the center of the track  
976 (see Figure 4.5). This function is strictly convex for  $\alpha \in \left(-\frac{\pi}{2}, \frac{\pi}{2}\right)$  and in our case,  
977 the center of the arc lies outside of the detector and  $\alpha$  is restricted to a small  
978 interval around zero (especially considering that the initial guess should make the  
979 fitted trajectory reasonably close to any relevant point, in the worst-case scenario,  
980 the distance is overestimated which should keep the fit from converging to such  
981 solutions).

982 In a more general case, if we consider the vector  $\mathbf{a}(\tau) = \mathbf{P} - \mathbf{X}(\tau)$  whose size  
983 is  $\|\mathbf{a}(\tau)\| = d_{\mathbf{P}}(\tau)$ , then we get

$$2d_{\mathbf{P}} \frac{dd_{\mathbf{P}}}{d\tau} = \frac{dd_{\mathbf{P}}^2}{d\tau} = \frac{d}{d\tau} \sum_i a_i^2 = 2 \sum_i a_i \frac{da_i}{d\tau} = 2\mathbf{a} \cdot \frac{d\mathbf{a}}{d\tau} = -2\mathbf{a} \cdot \frac{d\mathbf{X}}{d\tau}, \quad (4.30)$$

984 therefore for the derivative of  $d_{\mathbf{P}}(\tau)$  to be zero,  $\mathbf{a}(\tau)$  has to be perpendicular  
985 to the tangent of the track. In 3D, for a given  $\mathbf{X}(\tau)$ , this condition restricts  $\mathbf{P}$   
986 to a plane. This means that for a curving track we can find a point  $\mathbf{P}$  for any  
987 two points  $\mathbf{X}(\tau), \mathbf{X}(\sigma)$  with non-parallel tangents that has  $\frac{dd_{\mathbf{P}}}{d\tau}(\tau) = \frac{dd_{\mathbf{P}}}{d\tau}(\sigma) =$   
988  $= 0$ , which violates the assumption 4.28. If we have a circle-and-lines track as  
989 described in the previous sections, such a point has to lie outside of the circular  
990 sector given by the arc.

991 For a planar track, the envelope of all its normals is the evolute of the curve  
992 (i.e., the set of centers of all its osculating circles). If the track has a monotonous  
993 tangent angle

$$\alpha(\tau) = \text{atan} \frac{\frac{dX_2}{d\tau}}{\frac{dX_1}{d\tau}} \quad (4.31)$$

994 with minimal and maximal  $\alpha$  differing by less than  $\pi$  (i.e., the track changes  
995 direction by less than  $180^\circ$ ), then all intersections of the track's normals must lie  
996 on the side of the evolute closer to the track (not obvious?, sometimes the sides  
997 are opposite?). At the same time, the intersection must lie in the half planes  
998 given by the normals at the beginning and the end of the curve and pointing

999 away from the curve. Together, these three boundaries define a closed shape that  
1000 will lie outside of the OFTPC for a typical track in our detector.

1001 With the assumption 4.28, we can find the segment on the RK4 track with  
1002 the lowest distance to a given point  $\mathbf{P}$  using a binary search algorithm. Let  
1003 the distance of the point from the  $n$ -th vertex be  $d_{\mathbf{P},n}$ . Then the difference  
1004  $\Delta d_{\mathbf{P},n} = d_{\mathbf{P},n} - d_{\mathbf{P},n-1}$  satisfies

$$\begin{aligned}\Delta d_{\mathbf{P},n} &< 0 \quad \forall n \text{ such that } \tau_n < \tau_{\min}, \\ \Delta d_{\mathbf{P},n} &> 0 \quad \forall n \text{ such that } \tau_{n-1} > \tau_{\min}.\end{aligned}\tag{4.32}$$

1005 Therefore, we can search for the segment containing  $d_{\mathbf{P},\min}$  with binary search  
1006 starting with  $\Delta d_{\mathbf{P},1}$  and  $\Delta d_{\mathbf{P},N}$ , then calculate the difference  $\Delta d_{\mathbf{P},m}$  for the middle  
1007 index  $m = \left\lfloor \frac{N+1}{2} \right\rfloor$ . If  $\Delta d_{\mathbf{P},m} > 0$  (minor bug in the implementation – if the  
1008 value for the maximal index is negative, it shouldn't change anything), we can  
1009 replace the higher index with  $m$ , otherwise we replace the lower index. The search  
1010 stops when the difference between the minimal and maximal index is one. Would  
1011 it be better if they were the same (maybe not)? Then the minimal value is  
1012  $d_{\mathbf{P},n-1}$  or  $d_{\mathbf{P},N}$  and we can take the minimum of the distances from the two  
1013 segments connected to  $n-1$ . Currently taking the maximal index (and starting  
1014 at  $N-2$  maximal index  $\leftrightarrow N-1$ -th point), this should be equivalent, since either  
1015  $\Delta d_{\mathbf{P},\max} > 0$  (in the code is equivalent to max-1 here) or we are at  $N-1$ . The  
1016 minimum of the two distances still taken.

1017 Same details with MIGRAD etc. as previously.

### 1018 4.3.1 Testing on a microscopic sample

1019 The Runge-Kutta fit together with the 3D circle-and-lines pre-fit was tested  
1020 on a sample of tracks simulated using the microscopic simulation described in  
1021 Section 2.1. At first, few tracks with randomized initial parameters (same as  
1022 the Runge-Kutta sample in Section 2.2.1) were generated for preliminary testing.  
1023 Later, a sample with a grid-like distribution of track parameters was generated  
1024 (see Section 2.1.2 for details).

1025 Initial parameters of the HEED track (also should be in the first testing track  
1026 → subsection of microsim?). Initial parameters set in the circle fit (if electron set  
1027 alpha one way, otherwise other way) and parameter bounds.

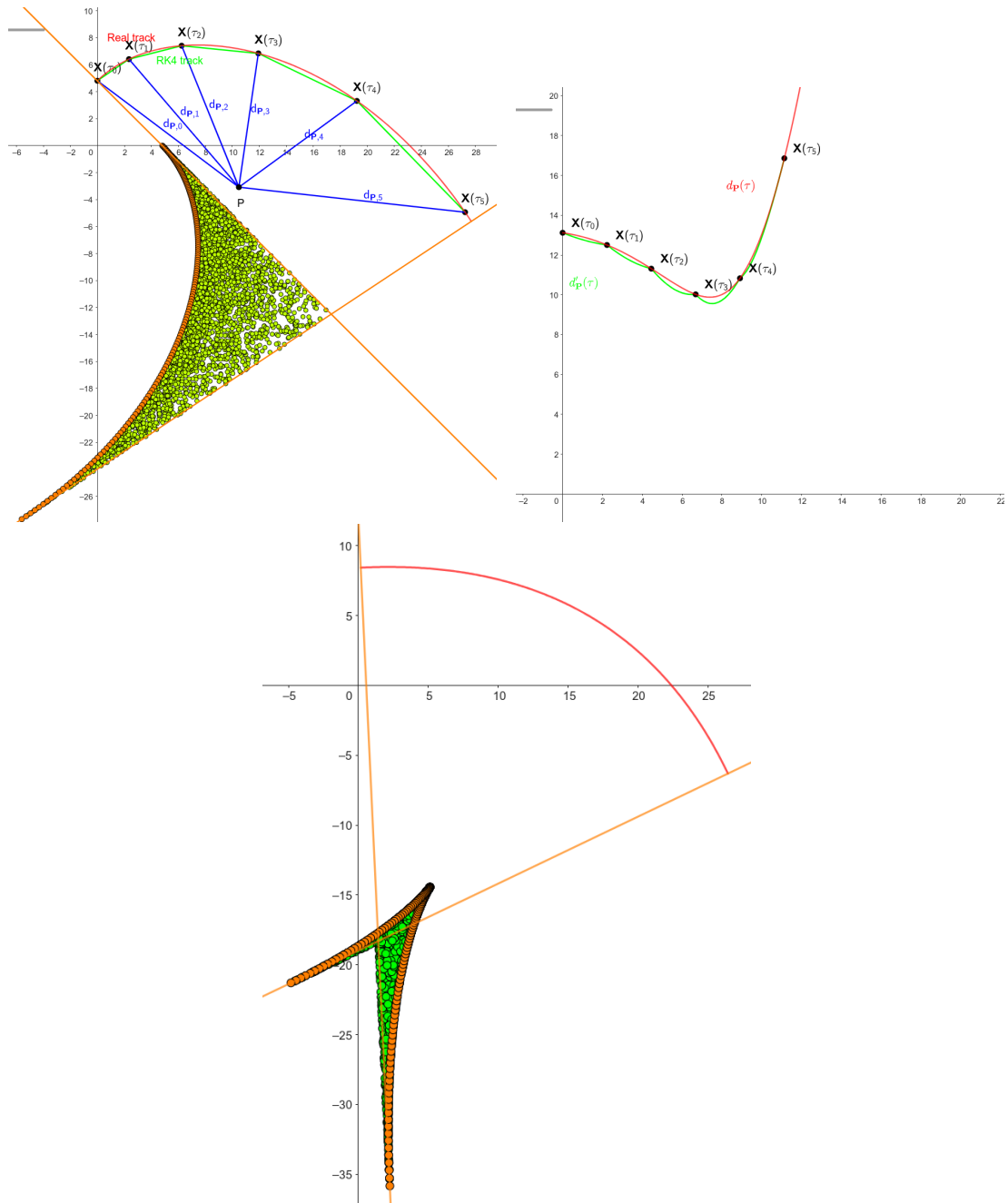


Figure 4.6: some provisional figures

# 1028 Conclusion

1029 Here or at the end of each section. Something about the future of this work?

1030

## 1031 Notes

1032 General notes about the thesis:

- 1033 • Check that all of the classes and other code are marked the same way in  
1034 the text. I used italics somewhere, could use different font for this instead.
- 1035 • Check unbreakable space in front of articles. Remove excessive article usage  
1036 with proper nouns.
- 1037 • Currently using margins for single-sided printing (bigger on the left side).
- 1038 • Check that present tense is used
- 1039 • Active vs passive voice usage
- 1040 • American English quotation marks (") instead of British English (').
- 1041 • Some of the overfull hbox warnings might change if duplex printing is used  
1042 (they generate black rectangles on the edge of the page), leaving them be  
1043 for now
- 1044 • Check nobreakdash usage (is it always necessary)
- 1045 • Check capitalized references (e.g., Figure, Section, Equation)
- 1046 • Check  $\backslash(...\backslash)$  math mode instead of  $\$...$$ . (actually unlike  $\backslash[...\backslash]$  math mode,  
1047 there is apparently no real benefit to this clumsy syntax)
- 1048 • Use siunitx package to ensure correct formatting, physics package for deriva-  
1049 tives.
- 1050 • Check other stuff that's written in the MFF UK template. Apparently it  
1051 has since been updated and there are some differences (check for them).
- 1052 • Check correct subscripts in equation (italics vs no italics)
- 1053 • Consistent bold marking of points/vectors
- 1054 • Correct footnotes (capital letters, etc.).
- 1055 • Might have to mention GeoGebra as per the non-commercial license agree-  
1056 ment (Made with GeoGebra®) – maybe put it into acknowledgments next  
1057 to the MetaCentrum credit? And list all of the figures where GeoGebra was  
1058 used?
- 1059 • Maybe make some section outside of References specifically for literature?  
1060 (such as the old CERN TPC review, ATOMKI review is currently not  
1061 mentioned, not sure if some Wikipedia articles should get a mention or how  
1062 do these things work)
- 1063 • Consistent use of `bm` vs `mathbf`

- Consistent use of  $\bar{\mathcal{M}}$  instead of  $\mathcal{M}$  when talking about the map of the means (so most of the time)
  - Proper equation numbering when deriving a relation
  - Hugo should be mentioned somewhere in the title pages probably?
  - Consistent itemize/enumerate style (namely spacing) that looks good (ideally set by some macro? maybe the new MFF UK template will solve this?)
  - Consistent gas mixture notation (e.g., 90:10 Ar:CO<sub>2</sub>). Maybe mention at the beginning that it is a molar ratio.
  - Labels of figures and tables – maybe in bold? Abbreviated?
- 1073 Random notes:
- Terminology consistency – ionization/primary/secondary electrons
  - Consistent TPC vs OFTPC acronym usage in the text or individual chapters.
  - Only electrons that start and end in the sector closer than 0.5 cm are used for reconstruction (newest version).
  - Attachment, Penning transfer and secondary ionization not considered in the microscopic simulation.
  - Suspicious artifacts of trilinear interpolation in Figure 1.7. **Fixed – integers instead of doubles in the implementation, influenced reconstruction SIGNIFICANTLY (but not simulation).**
  - Profiling of the reconstruction!!!! Find out what's taking the most time (probably Runge-Kutta integration which the fit calls a lot). Could gradually decrease the step size to refine the fit instead of making it small right away (arbitrarily small – the effect of this was never tested). This could take some time to do properly (find a profiler or make profiling macros).
  - Slow drift velocity good for  $z$  reconstruction, too low leads to recombination
  - Could add link to the GitHub repository, mention CMake? Details about simulating on MetaCentrum?
  - The first used track had 8 MeV momentum  $p = \gamma mv$  (not kinetic energy  $E_{\text{kin}} = (\gamma - 1)mc^2 = \sqrt{p^2c^2 + m^2c^4} - mc^2 \approx 7.5$  MeV)
  - Maybe cite Garfield++ user manual instead? Using TRandom3 for random number generation.
  - Does the RK fit error correlate with the actual error?

## 1097 Future

1098 Things planned for the future:

- Testing the reconstruction algorithm by measuring real particles with a known energy distribution.

- The **Fast Simulation with Ionization Electron Map** is planned for the future. It will use the HEED program [30] to simulate the primary particle and the Ionization Electron Map (see Section 3.2) to simulate the drift of secondary electrons. It should be significantly faster than the Microscopic Simulation but offer comparable precision since it will rely on an already simulated drift map. (Primary track simulated in HEED. Readout parameters by interpolating the map. Diffusion from the map for randomization.)
- Account for GEM, delta electrons, ...
- Likelihood approach instead of least squares (if it improves the reconstruction significantly), we should at least use a better method than taking the center of the TPC bin.
- More detailed electric field simulation (if needed, GEM will have more complex field, some irregularities in the field should be considered)
- Account for the triggering in MWPC/TPX3 (particle travels from TPX3 to MWPC basically immediately – fraction of a nanosecond so there should be no significant difference)

1117

## 1118 Likelihood - inverse map

1119 If we wanted to further improve this procedure, taking into account the whole  
 1120 map  $\mathcal{M}$ , we could make an "inverse map" from  $\mathcal{R}$  to distributions on  $\mathcal{D}$ . We could  
 1121 achieve this by taking the normalized probability density of an electron with initial  
 1122 coordinates  $(x, y, z)$  having readout coordinates  $(x', y', t)$ . If we fix  $(x', y', t)$ , we  
 1123 get an unnormalized probability density  $f(x, y, z) = \mathcal{M}_{(x,y,z)}(x', y', t)$  (assuming  
 1124 that all initial coordinates are a priori equally likely). This could potentially  
 1125 improve the discrete reconstruction if we take the mean value of this probability  
 1126 density across the pad and time bin

$$f_{\text{pad, bin}}(x, y, z) = \frac{1}{A_{\text{pad}} \Delta t_{\text{bin}}} \int_{\text{pad, bin}} \mathcal{M}_{(x,y,z)}(x', y', t) dx' dy' dt \quad (4.33)$$

1127 and using it for a likelihood fit instead of using least squares. This still assumes  
 1128 that all initial coordinates are equally likely which is clearly not the case for  
 1129 a primary particle track. In the future, we could even use the fast track simulation  
 1130 with the map (should be possible to make around 1000 tracks per minute per core  
 1131 with current settings), create a big set of tracks with reasonable parameters and  
 1132 use these to get an approximation of the probability distribution of the detector  
 1133 response. Some approximations would be necessary when interpreting the data to  
 1134 decrease the degrees of freedom of this distribution (we would have to pick a set of  
 1135 parameters and assume that some of them are independent). This could give us  
 1136 an idea about the best achievable resolution (how significantly will the detector  
 1137 response differ for a given change in energy). If the difference is significant, we  
 1138 could try to further improve the likelihood fit.

# Bibliography

1. *Garfield++* [<https://garfieldpp.web.cern.ch/garfieldpp/>]. [N.d.]. Accessed: 2023-05-18.
2. BRUN, Rene; RADEMAKERS, Fons. Root — An Object Oriented Data Analysis Framework. *Nucl. Instrum. Methods Phys. Res. Sect. A: Accel. Spectrom. Detect. Assoc. Equip.* 1997, vol. 389, no. 1–2, pp. 81–86. Available from DOI: 10.1016/s0168-9002(97)00048-x. Proceedings AIHENP'96 Workshop, Lausanne, Sep. 1996, See also <https://root.cern/>, Paper published in the Linux Journal, Issue 51, July 1998.
3. *About MetaCentrum* [<https://metavo.metacentrum.cz/en/about/index.html>]. 2023. Accessed: 2024-11-27.
4. ROSE, M. E. Internal Pair Formation. *Phys. Rev.* 1949, vol. 76, pp. 678–681. Available from DOI: 10.1103/PhysRev.76.678.
5. ESSIG, R. et al. *Dark Sectors and New, Light, Weakly-Coupled Particles*. 2013. Available from arXiv: 1311.0029 [hep-ph].
6. DE BOER, F.W.N. et al. A deviation in internal pair conversion. *Phys. Lett. B*. 1996, vol. 388, no. 2, pp. 235–240. ISSN 0370-2693. Available from DOI: [https://doi.org/10.1016/S0370-2693\(96\)01311-1](https://doi.org/10.1016/S0370-2693(96)01311-1).
7. BOER, F W N de et al. Excess in nuclear pairs near 9 MeV/ invariant mass. *J. Phys. G: Nucl. Part. Phys.* 1997, vol. 23, no. 11, p. L85. Available from DOI: 10.1088/0954-3899/23/11/001.
8. BOER, F W N de et al. Further search for a neutral boson with a mass around 9 MeV/c<sup>2</sup>. *J. Phys. G: Nucl. Part. Phys.* 2001, vol. 27, no. 4, p. L29. Available from DOI: 10.1088/0954-3899/27/4/102.
9. VITÉZ, Attila et al. Anomalous Internal Pair Creation in <sup>8</sup>Be as a Signature of the Decay of a New Particle. *Acta Phys. Pol. B - ACTA PHYS POL B*. 2008, vol. 39, p. 483.
10. KRASZNAHORKAY, A. et al. Searching for a light neutral axial-vector boson in isoscalar nuclear transitions. *Frascati Phys. Ser.* 2012, vol. 56, p. 86.
11. KRASZNAHORKAY, A. J. et al. Observation of Anomalous Internal Pair Creation in <sup>8</sup>Be: A Possible Indication of a Light, Neutral Boson. *Phys. Rev. Lett.* 2016, vol. 116, no. 4. ISSN 1079-7114. Available from DOI: 10.1103/physrevlett.116.042501.
12. TILLEY, D.R. et al. Energy levels of light nuclei A=8,9,10. *Nucl. Phys. A*. 2004, vol. 745, no. 3, pp. 155–362. ISSN 0375-9474. Available from DOI: <https://doi.org/10.1016/j.nuclphysa.2004.09.059>.
13. SAS, N. J. et al. *Observation of the X17 anomaly in the <sup>7</sup>Li(p,e<sup>+</sup>e<sup>-</sup>)<sup>8</sup>Be direct proton-capture reaction*. 2022. Available from arXiv: 2205.07744 [nucl-ex].
14. KRASZNAHORKAY, A. J. et al. New anomaly observed in <sup>4</sup>He supports the existence of the hypothetical X17 particle. *Phys. Rev. C*. 2021, vol. 104, no. 4. ISSN 2469-9993. Available from DOI: 10.1103/physrevc.104.044003.

- 1181 15. TILLEY, D.R. et al. Energy levels of light nuclei A = 4. *Nucl. Phys. A*.  
1182 1992, vol. 541, no. 1, pp. 1–104. ISSN 0375-9474. Available from DOI: [https://doi.org/10.1016/0375-9474\(92\)90635-W](https://doi.org/10.1016/0375-9474(92)90635-W).
- 1184 16. KRASZNAHORKAY, A. J. et al. New anomaly observed in  $^{12}\text{C}$  supports the  
1185 existence and the vector character of the hypothetical X17 boson. *Phys. Rev.*  
1186 *C*. 2022, vol. 106, p. L061601. Available from DOI: 10.1103/PhysRevC.106.  
1187 L061601.
- 1188 17. AJZENBERG-SELOVE, F. Energy levels of light nuclei A = 11,12. *Nucl. Phys.*  
1189 *A*. 1990, vol. 506, no. 1, pp. 1–158. ISSN 0375-9474. Available from DOI:  
1190 [https://doi.org/10.1016/0375-9474\(90\)90271-M](https://doi.org/10.1016/0375-9474(90)90271-M).
- 1191 18. KÁLMÁN, Péter; KESZTHELYI, Tamás. Anomalous internal pair creation.  
1192 *The Eur. Phys. J. A*. 2020, vol. 56. Available from DOI: 10.1140/epja/  
1193 s10050-020-00202-z.
- 1194 19. ALEKSEJEVS, A. et al. *A Standard Model Explanation for the "ATOMKI*  
1195 *Anomaly"*. 2021. Available from arXiv: 2102.01127 [hep-ph].
- 1196 20. FENG, Jonathan L. et al. Protophobic Fifth-Force Interpretation of the Ob-  
1197 served Anomaly in  $^8\text{Be}$  Nuclear Transitions. *Phys. Rev. Lett.* 2016, vol. 117,  
1198 p. 071803. Available from DOI: 10.1103/PhysRevLett.117.071803.
- 1199 21. ANH, Tran The et al. Checking the 8Be Anomaly with a Two-Arm Electron  
1200 Positron Pair Spectrometer. *Universe*. 2024, vol. 10, no. 4, p. 168. ISSN 2218-  
1201 1997. Available from DOI: 10.3390/universe10040168.
- 1202 22. ABRAAMYAN, Kh. U. et al. *Observation of structures at  $\sim 17$  and  $\sim 38$*   
1203 *MeV/c $^2$  in the  $\gamma\gamma$  invariant mass spectra in pC, dC, and dCu collisions at*  
1204 *p<sub>lab</sub> of a few GeV/c per nucleon*. 2023. Available from arXiv: 2311.18632  
1205 [hep-ex].
- 1206 23. THE MEG II COLLABORATION et al. *Search for the X17 particle in  $^7\text{Li}(p, e^+e^-)^8\text{Be}$*   
1207 *processes with the MEG II detector*. 2024. Available from arXiv: 2411.07994  
1208 [nucl-ex].
- 1209 24. ABED ABUD, Adam et al. A Gaseous Argon-Based Near Detector to En-  
1210 hance the Physics Capabilities of DUNE. 2022. Available from DOI: 10.  
1211 48550/arXiv.2203.06281.
- 1212 25. LOKEN, Stewart C. et al. Performance of the Signal Processing System for  
1213 the Time Projection Chamber. *IEEE Trans. on Nucl. Sci.* 1983, vol. 30, no.  
1214 1, pp. 162–166. Available from DOI: 10.1109/TNS.1983.4332243.
- 1215 26. HILDÉN, T. et al. Optical quality assurance of GEM foils. *Nucl. Instrum.*  
1216 *Methods Phys. Res. Sect. A: Accel. Spectrom. Detect. Assoc. Equip.* 2015,  
1217 vol. 770, pp. 113–122. ISSN 0168-9002. Available from DOI: 10.1016/j.j.  
1218 nima.2014.10.015.
- 1219 27. AHMED, Misbah Uddin. *Simulation of the electron and ion movement through*  
1220 *a 4-GEM stack*. 2021. Institut für Kernphysik.
- 1221 28. MARMELAD. *3D interpolation2.svg*. 2025. Available also from: [https://commons.wikimedia.org/wiki/File:3D\\_interpolation2.svg](https://commons.wikimedia.org/wiki/File:3D_interpolation2.svg). Licensed  
1222 under CC BY-SA 3.0 (<https://creativecommons.org/licenses/by-sa/3.0/legalcode>). Accessed: 9-April-2025.  
1223  
1224

- 1225 29. CMGLEE. *Trilinear interpolation visualisation*. 2025. Available also from:  
1226 [https://commons.wikimedia.org/wiki/File:Trilinear\\_interpolation\\_](https://commons.wikimedia.org/wiki/File:Trilinear_interpolation_visualisation.svg)  
1227 [visualisation.svg](https://commons.wikimedia.org/wiki/File:Trilinear_interpolation_visualisation.svg). Licensed under CC BY-SA 3.0 (<https://creativecommons.org/licenses/by-sa/3.0/legalcode>). Accessed: 26-March-2025.  
1228
- 1229 30. SMIRNOV, I.B. Modeling of ionization produced by fast charged particles in  
1230 gases. *Nucl. Instrum. Methods Phys. Res. Sect. A: Accel. Spectrom. Detect.*  
1231 *Assoc. Equip.* 2005, vol. 554, no. 1, pp. 474–493. ISSN 0168-9002. Available  
1232 from DOI: <https://doi.org/10.1016/j.nima.2005.08.064>.

1233 **Acknowledgments:** Computational resources were provided by the e-INFRA  
1234 CZ project (ID:90254), supported by the Ministry of Education, Youth and Sports  
1235 of the Czech Republic. **Figures that were drawn with GeoGebra. Maybe grant?**

# <sup>1236</sup> List of Figures

1237	0.1	The ATOMKI anomalous IPC measured for different nuclei. . . . .	5
1238	0.2	Results from the Hanoi spectrometer – angular $e^+e^-$ pair correlations measured in the ${}^7\text{Li}(p, e^+e^-){}^8\text{Be}$ reaction at $E_p = 1225$ keV [21]. . . . .	6
1239	0.3	Results from the MEG II experiments – angular correlation of $e^+e^-$ pairs with $E_{\text{sum}} \in [16, 20]$ MeV measured in the ${}^7\text{Li}(p, e^+e^-){}^8\text{Be}$ reaction with proton beam energies 500 and 1080 keV. The 500 keV dataset is fitted with Monte Carlo of both the IPC deexcitation and the EPC produced by gammas [23]. . . . .	7
1240	0.4	Schematics of the detector at the Van der Graaff facility at IEAP CTU. . . . .	7
1241	1.1	Particle identification in the PEP-4 TPC at SLAC based on the energy loss per distance $\frac{dE}{dx}$ [24]. . . . .	9
1242	1.2	Schematic view of the PEP-4 TPC [25]. A charged particle produced in a collision in the beam pipe creates a spiral ionization track in the magnetic field. The central cathode then accelerates ionization electrons towards the endcap anode wires where they are multiplied and read out. . . . .	10
1243	1.3	A scanning electron microscope image of a GEM foil [26]. . . . .	12
1244	1.4	Garfield simulation of an avalanche in a GEM hole [27]. An incoming electron (orange) is accelerated in the strong electric field of the GEM and causes further ionization multiplying the number of free electrons (orange). Most of the produced cations (red) are captured by the GEM cathode. . . . .	13
1245	1.5	Schematics of the first sector OFTPC with detector space coordinates. . . . .	15
1246	1.6	Pad layout of the OFTPC and its parameters. Pads 102, 124 and 127 are irregular, the rest has the same dimensions. . . . .	16
1247	1.7	Magnetic field simulation results. The OFTPC volume and the vacuum tube are marked with black lines, the magnets are marked with red lines. <b>The coordinates of the magnets from the CAD drawing seem to be 9/10 of the ones from the magnetic simulation (confirm and fix).</b> . . . . .	17
1248	1.8	Visualization of trilinear interpolation as a composition of linear interpolations (inspired by [28]). We want to interpolate the value in the red point C. First we interpolate between the four pairs of blue points sharing the last two indices along the $x$ -axis (Eq. 1.14), then between the two pairs of the resulting green points along the $y$ -axis (Eq. 1.15) and finally between the two resulting orange points along the $z$ -axis to get the final red value (Eq. 1.16). . . . .	18
1249	1.9	Geometric interpretation of trilinear interpolation as expressed in Equation 1.18. The colored dots represent the values in given points and the colored boxes represent the volume in the opposite corner by which the corresponding values are multiplied. The black dot represents the interpolated value which is multiplied by the entire volume [29]. . . . .	18

1281	2.1 Comparison of drift lines for two different gas mixtures 90:10 and 1282 70:30 Ar:CO <sub>2</sub> . The electron track is marked in black, the drift lines 1283 of the ionization electrons are marked in orange. In this example, 1284 we assume a larger OFTPC volume with readout at $z = 8$ cm. . . . .	21
1285	2.2 A visualization of a set of tracks from the grid-like testing sample 1286 with the same kinetic energy. . . . .	22
1287	2.3 A comparison of the HEED track from the microscopic simulation 1288 in Section 2.1.1 with a Runge-Kutta track with the same initial 1289 parameters and $\tau_{\text{step}} = 0.1$ ps (reducing the step further doesn't 1290 make a visible difference). In the view of the tracks on the left, 1291 the distance of the HEED ionization electrons from the RK4 track 1292 is exaggerated 1000 $\times$ . On the right, the dependence of the HEED 1293 electrons residuals (i.e., their shortest distance to the RK4 track) 1294 on their $z$ -coordinate is shown. <b>The images look the same even for 1295 100,000x smaller step, so the residuals are a result of something 1296 that HEED does.</b> . . . . .	24
1297	3.1 Linear fit of the drift time $t$ dependence on the distance to the 1298 readout $d_r = 8$ cm – $z$ for the ionization electrons in 90:10 (left) 1299 and 70:30 (right) Ar:CO <sub>2</sub> gas composition. Only electrons inside 1300 the TPC (red) are fitted. The parameters are $v_d = 3.39$ cm/ $\mu$ s, 1301 $d_0 = -0.41$ cm for 90:10, and $v_d = 0.939$ cm/ $\mu$ s, $d_0 = -0.11$ cm 1302 for 70:30 Ar:CO <sub>2</sub> . . . . .	26
1303	3.2 Reconstruction (black) of the starting position of ionization elec- 1304 trons (red) using parameters obtained from the fit (Figure 3.1). 1305 Two gas compositions 90:10 (left) and 70:30 Ar:CO <sub>2</sub> (right) are 1306 compared. . . . .	27
1307	3.3 Comparison of residuals (i.e., the distance from the reconstructed 1308 point to the simulated ionization electron starting point) depen- 1309 dence on $x$ for two gas mixtures 90:10 (red) and 70:30 Ar:CO <sub>2</sub> 1310 (blue). . . . .	27
1311	3.4 Example of map generation. <b>Swap for better image, correct coor-</b> 1312 <b>dinates.</b> . . . . .	30
1313	3.5 Example reconstruction with the map. <b>Swap for better image, cor-</b> 1314 <b>rect coordinates.</b> . . . . .	30
1315	3.6 Selection of the points for interpolation. <b>Create better images; use 1316 the explanation interpolation vs. extrapolation strange property. 1317 Solution 2 probably does not make much sense.</b> . . . . .	33
1318	4.1 Example of a fitted reconstructed track. <b>Swap for better image.</b> . .	35
1319	4.2 First attempt at a track reconstruction using only the drift velocity. 1320 Spline energy reconstruction attempt. <b>Swap for better image(s) – 1321 subfigure environment, correct coordinates.</b> . . . . .	37
1322	4.3 First attempt at a track reconstruction using only the drift veloc- 1323 ity. Circle and Lines Fit in 2D. <b>Swap for better image, correct 1324 coordinates. Bias should be described in the previous chapter, not 1325 here.</b> . . . . .	39
1326	4.4 Circle and Lines Fit 3D geometry. <b>Swap for better image.</b> . . . . .	42

1327	4.5 Demonstration of the convexity of the distance function $d(\alpha)$ for	
1328	a circular track (see Equation 4.29). . . . .	43
1329	4.6 some provisional figures . . . . .	45

<sup>1330</sup> **List of Tables**

# <sup>1331</sup> List of Abbreviations

- <sup>1332</sup> **GEM** Gas Electron Multiplier
- <sup>1333</sup> **HEED** High Energy Electro-Dynamics
- <sup>1334</sup> **IEAP CTU** Institute of Experimental and Applied Physics, Czech Technical  
<sup>1335</sup> University in Prague
- <sup>1336</sup> **IPC** Internal Pair Creation
- <sup>1337</sup> **EPC** External Pair Creation
- <sup>1338</sup> **Micromegas** MICRO-MEsh GAseous Structure
- <sup>1339</sup> **MWPC** Multi-Wire Proportional Chamber
- <sup>1340</sup> **OFTPC** Orthogonal Fields TPC
- <sup>1341</sup> **RK4** Runge-Kutta 4th order
- <sup>1342</sup> **TPC** Time Projection Chamber
- <sup>1343</sup> **ToA** time-of-arrival
- <sup>1344</sup> **ToT** time-over-threshold
- <sup>1345</sup> **TPX3** Timepix 3